Gravity-Induced Collisions of Uncharged Cloud Droplets in an Electric Field

PIJUSH PATRA[a] AND ANUBHAB ROY[a]

[a] *Department of Applied Mechanics, Indian Institute of Technology Madras, Chennai, Tamil Nadu, India*

(Manuscript received 12 March 2025, in final form 9 July 2025, accepted 5 August 2025)

ABSTRACT: We theoretically study the collision dynamics of uncharged, conducting droplets settling under the influence of gravity in the presence of an external electric field. Our study demonstrates that the attractive forces induced by an external electric field can overcome lubrication resistance, facilitating surface-to-surface contact between two spherical conductors within a finite time. For water droplets moving in air, continuum lubrication theory fails when the gap between droplets becomes less than the mean free path of air molecules. To account for this, we incorporate noncontinuum lubrication effects in the collision calculations. By numerically computing the relative trajectories of the droplets, we assess how collision efficiency depends on the droplet size ratio, noncontinuum lubrication effects, the angle between the electric field and gravity, electric field strength, and van der Waals forces. Our findings reveal that electric field–induced forces significantly enhance collision efficiency, highlighting their critical role in droplet collision dynamics.

KEYWORDS: Atmospheric electricity; Cloud droplets; Cloud microphysics; Collisions; Drop size distribution

1. Introduction

The initiation of warm rain has long been a subject of interest in the cloud microphysics community, with a central question being: What mechanisms govern the evolution of droplet size distributions (DSDs) in atmospheric clouds (Pruppacher and Klett 1997; Devenish et al. 2012)? Growth through condensation alone is unlikely to produce the broad droplet size spectrum observed in in situ measurements (Prabha et al. 2011; Khain et al. 2013). Consequently, collisions and subsequent coalescence between droplets are the primary drivers of rain formation in warm clouds, with DSD evolution heavily dependent on the collision rate. Extensive research has examined the role of turbulence and gravitational settling in droplet collisions (see Shaw 2003; Grabowski and Wang 2013 and references therein). However, relatively few studies have investigated the influence of electrostatic forces on these interactions (Schlamp et al. 1976; Tinsley et al. 2000; Khain et al. 2004; Patra et al. 2023; Dubey et al. 2024). Incorporating an accurate parameterization of electrostatic forces into large-scale models, such as numerical weather prediction simulations, could enhance forecasting accuracy. More importantly, electrostatic forces may play a crucial role in initiating collisions among small droplets, introducing size disparities necessary for further growth. This study focuses on droplet collisions driven by electrostatic forces arising from an external electric field.

Most clouds are naturally electrified, making electrostatic interactions between cloud droplets a significant factor in the collision–coalescence process (Pruppacher and Klett 1997; Wang 2013). A vertically downward fair-weather electric field exists due to the potential difference between Earth's surface and the upper atmosphere. In thunderclouds, this electric field intensifies rapidly due to charge separation, driven by various charging mechanisms broadly categorized as convective, inductive, and noninductive (Kamra 1975; Latham 1981; Williams et al. 1989; Saunders 1993; Mareev and Dementyeva 2017). Detailed discussions on these mechanisms can be found in chapter 18.5 of Pruppacher and Klett (1997) and chapter 14.4 of Wang (2013). Laboratory experiments have consistently demonstrated that collisional charging during ice–ice collisions plays a crucial role in thundercloud electrification (Reynolds et al. 1957; Latham and Stow 1965; Takahashi 1978; Gaskell and Illingworth 1980; Jayaratne et al. 1983; Mason and Dash 2000; Saunders et al. 2006; Turner and Stow 2022). These findings have inspired the development of several theoretical models for collisional charging (Baker and Dash 1989, 1994; Dash et al. 2001; Dash and Wettlaufer 2003; Jungwirth et al. 2005; Kang et al. 2023).

The strength of the electric field in fair-weather clouds typically ranges from 10^2 to 10^3 V m^{-1}. However, field measurements (see Gunn 1948; chapter 18 of Pruppacher and Klett 1997; chapter 3 of Rakov and Uman 2003; Trinh et al. 2020) indicate that electric fields in highly electrified clouds can reach magnitudes of $O(10^4 - 10^5)$ V m^{-1}. Winn et al. (1974) even reported values as high as 4×10^5 V m^{-1}. Notably, these field studies suggest that the electric field is not always directed vertically downward; it can also act horizontally or at an oblique angle relative to gravity.

Strong electric fields in thunderclouds can significantly influence droplet collision dynamics. Recent field observations by Mudiar et al. (2018, 2021) suggest that intense electric fields in highly electrified clouds enhance raindrop growth and increase rainfall rates. Additionally, a series of wind tunnel experiments by Kamra and coworkers demonstrate that strong electric fields substantially alter the microphysical properties of electrified clouds, particularly affecting binary collisions between water droplets by modifying their impact velocities and deformation characteristics (Bhalwankar and Kamra 2007, 2009; Bhalwankar et al. 2023; Pawar et al. 2024).

Pijush Patra's current affiliation: Nordita, KTH Royal Institute of Technology and Stockholm University, Stockholm, Sweden

Corresponding author: Anubhab Roy, anubhab@iitm.ac.in

DOI: 10.1175/JAS-D-25-0040.1

An applied electric field, no matter how weak, induces electric charges of opposite signs on the nearest sides of two uncharged conducting droplets. As the droplets move closer, the mutual interactions between these induced charges enhance the local electric field in the region between the two droplets. This locally amplified electric field surpasses the strength of the imposed field, resulting in an increase in electrostatic attraction force as the droplets approach each other (Davis 1964). Notably, this electric field–induced attractive force between two uncharged conducting droplets increases without bound as their separation approaches zero (Lekner 2011a, 2013). As a result, this force could overcome lubrication resistance, facilitating surface-to-surface contact between droplets. However, it is important to note that the electric field–induced force diminishes significantly at larger droplet separation distances. Thus, two widely separated cloud droplets subject to an external electric field are unlikely to make contact unless influenced by a background flow, gravity, or thermal fluctuations that drive them into closer proximity.

The calculation of the electrostatic force between two uncharged or charged spherical droplets subject to an external electric field has been thoroughly investigated. One of the pioneering studies on this topic was carried out by Davis (1964), who calculated the electrostatic forces on two charged spherical conductors subject to an external electric field by integrating the electrical stresses over their surfaces. This electric stress is directly related to the gradient of the electric potential Φ_{el}. Davis (1964) determined the variation in the potential field by solving the Laplace equation for Φ_{el} in a bispherical coordinate system. For uncharged conducting spheres, the electrostatic forces depend on sphere sizes, the magnitude of the imposed electric field, the angle between the line joining the centers and the direction of the electric field, and the force coefficients F_1, F_2, and F_8 (Davis 1964). The expressions of these force coefficients involve infinite series summations. The convergence of these series becomes extremely slow for small separation distances. To avoid this issue, Lekner (2013) calculated the electric field–induced forces using the energy method, where he wrote the electrostatic energy of the system in terms of a polarizability tensor. Longitudinal and transverse polarizabilities are sufficient to describe the system energy and forces in the case of a two-sphere system. To obtain the electric field–induced forces in the close approach of two arbitrary-sized spherical conductors, we utilize the work of Lekner (2011b), who derived the exact analytical expressions for the longitudinal and transverse polarizabilities for small separation distances. The forces acting along the line joining two centers are equal and opposite and depend on the partial derivatives of these polarizabilities with respect to the separation distance. The forces normal to the line of centers produce torque on the two-sphere system, which depends on the difference between the longitudinal and transverse polarizabilities. This torque always acts to align the line of centers with the direction of the external electric field.

Droplet volume fractions in atmospheric clouds are typically low [about $O(10^{-6})$] (Grabowski and Wang 2013), and therefore, we focus exclusively on binary collisions. The rate equation for the droplet number density when two species are present is

$$-\frac{dn_1}{dt} = -\frac{dn_2}{dt} = K_{12}, \tag{1}$$

where K_{12} is the collision rate between droplet categories of number densities n_1 and n_2. Smoluchowski (1918) was the first to study the ideal collision rate for two noninteracting spheres settling under gravity in a quiescent fluid. The theoretical study of the droplet collision rate with hydrodynamic and nonhydrodynamic interactions is a challenging task. These interactions alter the collision rate by modifying the relative velocity between the droplet pair at close separations. The collision efficiency, which is the ratio of the collision rate with interactions to that obtained ignoring interactions (i.e., the ideal collision rate), captures the effects of interactions on the collision rate. Davis (1984) and Melik and Fogler (1984) predicted the collision efficiency for two unequal-sized rigid spheres sedimenting due to gravity and interacting via continuum hydrodynamics and van der Waals forces. Zhang and Davis (1991), Rother et al. (2022), and Ababaei and Rosa (2023) calculated the collision efficiency induced by interfacial mobilities for two differentially sedimenting viscous drops without and with inertial effects. Previous studies have utilized the work of Davis (1964) to analyze the collision rate of uncharged or charged sedimenting cloud droplets in an external electric field (Sartor 1960; Plumlee and Semonin 1965; Semonin and Plumlee 1966; Schlamp et al. 1976; Guo and Xue 2021). These studies do not resolve the full hydrodynamics across all separations, particularly in the lubrication regime where the gap between the surfaces of two spheres becomes much smaller than their radii. As a result, they fail to accurately capture the details of the collision process. Considering the internal circulation of fluid droplets, Zhang et al. (1995) predicted the electric field-enhanced collision rate of two uncharged conducting spherical droplets settling under gravity. However, these works did not account for the exact analytical form of electric field–induced forces in the lubrication regime. Recently, Thiruvenkadam et al. (2023) have analyzed relative trajectories of two arbitrary-sized uncharged conducting spheres without gravity and showed that because of the divergent nature of the electric field–induced forces in the lubrication regime, spheres could come into contact in a finite time. Motivated by this, we examine the effects of electric field–induced forces on pair trajectories and the collision rate of two uncharged conducting droplets sedimenting in still air.

This study does not account for the deformation of spherical droplets during their motion. We assume that the fluid motion induced by a settling pair of droplets is sufficiently slow such that the surrounding disturbance flow field satisfies the Stokes equations for creeping flow. We also ignore the inertia of the droplets because of their small size. However, the droplets are large enough for the influences of Brownian diffusion to be considered negligible in the collision dynamics. In section 2, we will provide justifications for these assumptions in the context of small cloud droplets.

When the separation distance between the surfaces of two droplets is comparable to or less than the radius of the smaller droplet, the interaction between them significantly disturbs the fluid velocity field around each other. These disturbances

give rise to additional hydrodynamic resistance on each droplet. This way, droplets interact with each other through the fluid medium. These hydrodynamic interactions between the droplets can significantly modulate the collision dynamics. Hydrodynamic interactions between a pair of droplets in Stokes flow conditions are well studied (see Guazzelli and Morris 2011; Kim and Karrila 2013). This hydrodynamic resistance is $O[1/f(\xi)]$ in the lubrication region, where ξ is the dimensionless (nondimensionalized by the average radius of the two interacting droplets) closest distance between the surfaces of the two droplets. The function $f(\xi) = \xi$ for two rigid spherical particles with continuum hydrodynamic interactions (Batchelor and Green 1972) and $f(\xi) = \sqrt{\xi}$ for two spherical viscous drops interacting via continuum hydrodynamics (Davis et al. 1989). For particles interacting in a gaseous medium, the continuum lubrication approximation would no longer be valid when the gap thickness between two surfaces is less than the mean free path of the medium λ_0, and then, one needs to consider noncontinuum lubrication resistance where $f(\xi) = \ln[\ln(\mathrm{Kn}/\xi)]/\mathrm{Kn}$ (Sundararajakumar and Koch 1996). Here, the Knudsen number (Kn) is defined as the ratio of the mean free path of the medium to the mean radius of the droplets. Previous studies have obtained collision rates due to noncontinuum interactions for droplets subject to the Brownian motion (Patra and Roy 2022), differential sedimentation and uniaxial compressional flow (Dhanasekaran et al. 2021b), simple shear flow (Patra et al. 2022), and turbulent flow (Dhanasekaran et al. 2021a).

We organize the paper as follows. In section 2, we will formulate the problem and outline the procedure for calculating the collision rate and efficiency using trajectory analysis. Then, in section 4, we will calculate the collision efficiency of a pair of hydrodynamically interacting droplets due to the combined effect of gravity, electric field, and van der Waals forces. Finally, in section 5, we will summarize our results and discuss their implications.

2. Problem formulation

a. The relative velocity between a pair of droplets

We consider two uncharged, conducting cloud droplets settling under gravity while subjected to a uniform external electric field inclined at an angle η relative to the gravitational direction. Hydrodynamic interactions between the droplets are also accounted for. In dilute systems like clouds, the probability of a third droplet significantly influencing the relative motion of two interacting droplets is negligible. Therefore, our analysis focuses on binary collisions.

In this analysis, we define the characteristic length, velocity, and time scales as $a^* = (a_1 + a_2)/2$, $V_{12}^{(0)} = |\mathbf{V}_{12}^{(0)}|$, and $a^*/V_{12}^{(0)}$, respectively. The relative velocity between two noninteracting spherical droplets that are settling under the influence of gravity in a quiescent medium is given by $\mathbf{V}_{12}^{(0)} = 2(\rho_p - \rho_f)(a_1^2 - a_2^2)\mathbf{g}/(9\mu_f)$, where a_1 is the radius of the larger droplet, a_2 is that of the smaller droplet, ρ_p and ρ_f are the droplet and fluid densities, respectively, $\mathbf{g}$ is the gravitational acceleration with its magnitude g, and μ_f is the dynamic viscosity of the fluid. Two key quantities that describe the relative geometry of the two spherical droplets are the size ratio $\kappa = a_2/a_1$ and the center-to-center distance r between the droplets. The dimensionless surface-to-surface distance ξ, which we used in the previous section, is defined as $\xi = [r - (a_1 + a_2)]/a^* = (r/a^*) - 2$.

Before proceeding further, it is important to justify the key assumptions made in this study. The characteristic hydrodynamic and electric stresses for a spherical water droplet sedimenting in air and subjected to an electric field are given by $\mu_f U_s/a$ and $\epsilon_0 E_0^2$, respectively. Here, a denotes the radius of the droplet, U_s represents the Hadamard–Rybczynski settling speed, defined as $U_s = 2[(\rho_p - \rho_f)ga^2/3\mu_f](\hat{\mu} + 1)/(3\hat{\mu} + 2)$ with $\hat{\mu}$ being the ratio of viscosities of droplet to the surrounding air, ϵ_0 denotes the permittivity of air, and E_0 is the magnitude of the external electric field. The capillary number (Ca), defined as $\mathrm{Ca} = \mu_f U_s/\gamma$, where γ is the surface tension at the air–water interface, measures the relative strength of hydrodynamic and capillary stresses. Similarly, the electric capillary number Ca_E, given by $\mathrm{Ca}_E = \epsilon E_0^2 a/\gamma$, quantifies the relative significance of electric and surface tension stresses. These two dimensionless parameters effectively characterize the deformation behavior of the droplet. Let us consider a water droplet in air with $a = 10\ \mu\mathrm{m}$, $\rho_p \approx 10^3\ \mathrm{kg\ m^{-3}}$, $\rho_f \approx 1\ \mathrm{kg\ m^{-3}}$, $\mu_f \approx 1.8 \times 10^{-5}\ \mathrm{Pa\ s}$, $\hat{\mu} \approx 10^2$, $E_0 = 10^5\ \mathrm{V\ m^{-1}}$, $\epsilon_0 = 8.85 \times 10^{-12}\ \mathrm{F\ m^{-1}}$, and $\gamma \approx 72 \times 10^{-3}\ \mathrm{N\ m^{-1}}$. Using these data, we find that $\mathrm{Ca} \approx 3 \times 10^{-6}$ and $\mathrm{Ca}_E \approx 1.2 \times 10^{-5}$ are sufficiently small, and thus, we can safely neglect droplet deformation. Furthermore, as $\hat{\mu} = O(10^2)$ for water droplets in air, the mobility of droplet interfaces is insignificant, which implies that small droplets will behave almost like rigid spherical particles.

The present study also ignores the role of flow and droplet inertia and thermal fluctuations in collision dynamics. We define the droplet Reynolds number (Re_p) based on the terminal settling speed and radius of the larger droplet: $\mathrm{Re}_p = [2\rho_f(\rho_p - \rho_f)ga_1^3]/(9\mu_f^2)$. The Stokes number, denoted as St, captures the droplet inertia and is defined as $\mathrm{St} = [16\rho_p(\rho_p - \rho_f)g(a_1^2 - a_2^2)(a_1a_2)^{3/2}]/[81\mu_f^2(a_1 + a_2)^2]$ (Davis 1984). The Péclet number Pe is given by $\mathrm{Pe} = 2\pi(\rho_p - \rho_f)a_1^4\kappa(1 - \kappa^2)g/(3k_BT)$, which measures the relative strengths of gravitational advection and diffusion induced by thermal fluctuations (Zinchenko and Davis 1994). Here, $k_B = 1.318 \times 10^{-23}\ \mathrm{J\ K^{-1}}$ is the Boltzmann constant and T is the absolute temperature. For water droplets in a warm cloud at $T = 273$ K with $a_1 = 10\ \mu$m, we obtain the following representative values: $\mathrm{Re}_p \approx 0.007$, $\mathrm{St} \approx 0.54$ for $\kappa = 0.3$ and $\mathrm{St} \approx 0.03$ for $\kappa = 0.99$, and $\mathrm{Pe} \approx 1504$ for $\kappa = 0.3$ and $\mathrm{Pe} \approx 1085$ for $\kappa = 0.99$. These typical values of Re_p and Pe support our assumption that flow inertia and thermal fluctuations can be considered negligible for the contexts examined. The representative St values suggest that droplet inertia is negligible for nearly equal-sized droplet pairs with radii less than 15 μm. In warm cumulus clouds, condensation is the primary mechanism for droplet growth up to 15 μm in radius, leading to a nearly monodisperse size distribution. Therefore, our assumption of negligible particle inertia is valid at the lower end of the size gap of 15–40 μm droplets. Our noninertial collision calculations will serve as reference calculations for future research in this field.

The collisional time scale, denoted as τ_{coll}, for two differentially sedimenting droplets can be mathematically expressed as $\tau_{\text{coll}} = a^*/V_{12}^{(0)}$. For water droplets dispersed in air, $\tau_{\text{coll}} \approx 8 \times 10^{-4}$ s when $a_1 = 10$ μm and $a_2 = 5$ μm. On the other hand, the droplet polarization time scale $\tau = \epsilon_0/\sigma \approx 6.5$ min, where $\sigma \approx 2.3 \times 10^{-14}$ S m^{-1} is the conductivity of clear air at sea level. It is important to note that in warm clouds, the conductivity of air can vary significantly, ranging from 1/40 to 1/3 of the fair-weather sea level conductivity (Pruppacher and Klett 1997). As a result, τ for typical cloud droplets may vary between approximately 20 min and 2 h. Given that $\tau_{\text{coll}} \ll \tau$, it is reasonable to neglect the influence of surface charge convection on the collision dynamics of the droplets.

The assumptions mentioned above greatly simplify our problem formulation. To describe the relative motion, we track the velocity of a satellite droplet (radius a_1) with respect to a test droplet (radius a_2) (see Fig. 1a). The relative velocity between the droplets is given by $\mathbf{V}_{12} = \mathbf{V}_1 - \mathbf{V}_2$. In the Stokesian regime, we can express the resultant relative velocity as a vector sum of contributions from gravity, electric field–induced forces, and van der Waals forces (Batchelor 1976, 1982; Davis 1984; Zhang et al. 1995):

$$\mathbf{V}_{12}(\mathbf{r}) = \mathbf{V}_{12}^{(0)}\left[L\frac{\mathbf{rr}}{r^2} + M\left(\mathbf{I} - \frac{\mathbf{rr}}{r^2}\right)\right] + \frac{1}{6\pi\mu_f}\left(\frac{1}{a_1} + \frac{1}{a_2}\right)\left[G\frac{\mathbf{rr}}{r^2} + H\left(\mathbf{I} - \frac{\mathbf{rr}}{r^2}\right)\right](\mathbf{F}_E + \mathbf{F}_{\text{vdW}}), \tag{2}$$

where $\mathbf{r}$ is the vector from the center of droplet 2 (test droplet) to the center of droplet 1 (satellite droplet) and $r = |\mathbf{r}|$. Here, $\mathbf{I}$ denotes the unit second-order tensor, while $\mathbf{F}_E$ and $\mathbf{F}_{\text{vdW}}$ represent the electric field–induced and van der Waals forces, respectively.

The mobility functions L and M characterize the relative motion of two settling droplets under gravity, with L governing motion along the line of centers and M governing motion perpendicular to it (Batchelor 1982). Similarly, G and H represent the corresponding mobility functions for droplets influenced by nonhydrodynamic forces. These functions depend on κ and ξ. To compute these mobility functions, we leverage the work of Wang et al. (1994) and Zinchenko and Davis (1994), who determined axisymmetric mobilities for continuum hydrodynamic interactions by solving the Stokes equations in a bispherical coordinate system. Additionally, we use the twin multipole expansion method developed by Jeffrey and Onishi (1984) to determine asymmetric mobilities. However, as the separation between droplet surfaces decreases, these series solutions require an increasingly large number of terms to achieve convergence, making them computationally inefficient. When the gap between the droplets becomes small, lubrication approximations for the mobility functions, available in the existing literature (Batchelor 1982; Jeffrey and Onishi 1984), provide a more efficient alternative.

In a continuum framework, hydrodynamic interactions prevent the surface-to-surface contact between two rigid spheres

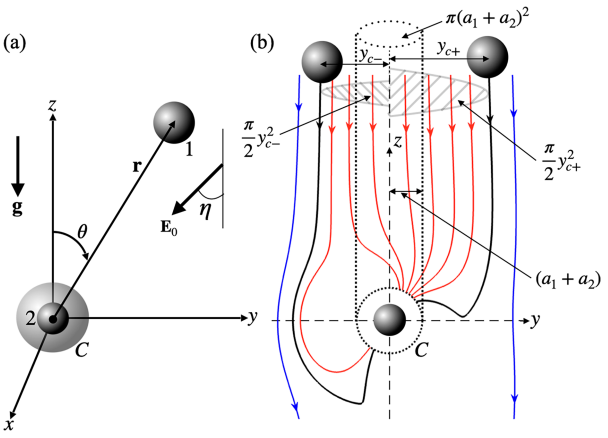

FIG. 1. (a) Schematic of the coordinate system used in the analysis. Here, "1" indicates the sphere with radius a_1 and "2" indicates the sphere with radius a_2. The sphere marked "C" is the collision sphere of radius $a_1 + a_2$. The electric field $\mathbf{E}_0$ makes an angle η with the gravity direction. (b) Schematic of upstream collisional areas. The red, black, and blue lines represent colliding, limiting, and open trajectories, respectively. The dotted circle with a radius of $a_1 + a_2$ denotes the upstream interception area for a noninteracting droplet pair. Additionally, the two hatched semicircles, with radii y_{c+} and y_{c-} on the positive and negative sides of the y axis, respectively, illustrate the upstream interception areas that define the actual collision rate.

within a finite time unless an attractive nonhydrodynamic force, such as van der Waals forces, is present. However, even in the absence of such forces, noncontinuum lubrication effects can enable collisions to occur in finite time. This arises because the resistance functions associated with motion along the line connecting the two droplet centers exhibit a weaker divergence rate in the noncontinuum regime (Dhanasekaran et al. 2021b; Patra and Roy 2022). Sundararajakumar and Koch (1996) derived expressions for noncontinuum lubrication forces for axisymmetric motion. Building on this work, Dhanasekaran et al. (2021b) have recently incorporated noncontinuum lubrication effects into the axisymmetric mobility functions. Their approach treats lubrication interactions as continuum for $\xi > O(\text{Kn})$ and noncontinuum for $\xi \leq O(\text{Kn})$, where the Knudsen number $\text{Kn} = \lambda_0/a^*$ captures the significance of noncontinuum interactions. In this study, we adopt the uniformly valid solutions for L and G developed by Dhanasekaran et al. (2021b). For asymmetric mobilities M and H, continuum hydrodynamics provides a reasonable approximation at all separations because these mobility functions approach a finite value as $\xi \to 0$. Consequently, continuum breakdown is not expected to significantly affect asymmetric relative motions for an inertialess droplet pair, allowing us to use continuum hydrodynamics for asymmetric mobilities throughout. However, when calculating the collision rate for an inertial droplet pair in a gaseous medium, noncontinuum lubrication effects must also be considered for relative motions in the tangential directions (Li Sing How et al. 2021).

The calculation of electrostatic forces between two conducting droplets in an external electric field is primarily a boundary value problem where one needs to solve Laplace's

equation for the potential field in a bispherical coordinate system (Davis 1964). Once the potential field is determined, the electric field–induced forces on each droplet can be obtained by integrating the electrical stresses over their surfaces. In this case, the forces acting on the two droplets are equal and opposite. Given the axisymmetric nature of the problem, the force on each droplet can be decomposed into two components: one directed along the line of centers and the other perpendicular to it. The expressions for the electric field–induced forces in r and θ directions are given by Davis (1964):

$$F_E^r = -4\pi\epsilon_0 a_2^2 E_0^2 [F_1 \cos^2(\theta - \eta) + F_2 \sin^2(\theta - \eta)], \quad (3)$$

$$F_E^\theta = 4\pi\epsilon_0 a_2^2 E_0^2 F_8 \sin 2(\theta - \eta), \quad (4)$$

where $(\theta - \eta)$ is the angle between the electric field vector $\mathbf{E}_0$ and the line joining the centers of two spheres, and F_1, F_2, F_8 are the force coefficients that depend on the center-to-center distance and the size ratio of the two droplets. The analytical expressions for these force coefficients in the near and far fields are provided in Thiruvenkadam et al. (2023).

The van der Waals attraction force always acts along the line joining the centers of the two droplets, and therefore, we can write $F_{\mathrm{vdW}} = -d\Phi_{\mathrm{vdW}}/dr$, where Φ_{vdW} is the van der Waals potential. Hamaker (1937) derived an analytical expression for the unretarded form of Φ_{vdW} using a pairwise additivity theory. However, Hamaker's analysis did not consider the effects of retardation due to the finite propagation speed of electromagnetic waves. One must consider the effects of retardation when separation is comparable to or more than the London wavelength λ_L(≈0.1 μm). In the present analysis, we use the work of Zinchenko and Davis (1994), who obtained the retarded van der Waals potential by integrating the dispersion energy between two molecules. The functional form of Φ_{vdW} depends on the dimensionless center-to-center distance, the size ratio, the nondimensional quantity N_L defined as the radius of the droplets scaled with λ_L [i.e., $N_L = 2\pi(a_1 + a_2)/\lambda_L = 2\pi a_1(1 + \kappa)/\lambda_L$], and the Hamaker constant A_H.

We begin our analysis by expressing the relative velocity $\mathbf{V}_{12}$ in a spherical coordinate system (r, θ, ϕ) with its origin located at the center of the test droplet. To simplify the analysis, we nondimensionalize the governing equation using the characteristic length, velocity, and time scale pertinent to this problem. As the characteristic length scale is defined as $a^* = (a_1 + a_2)/2$, the range of nondimensional radial separations between the centers of the two droplets varies from 2 to ∞. From now on, we use the notation r as the nondimensional radial distance between the centers of the two droplets. The sphere with a dimensionless radius of $r = 2$ is referred to as the collision sphere, labeled as sphere C in Fig. 1a. Conversely, at $r = \infty$, one droplet does not influence the other. We denote the nondimensional coordinates with an overbar such that $\bar{x} = x/a^*$, $\bar{y} = y/a^*$, and $\bar{z} = z/a^*$ represent the dimensionless coordinates. The size ratio κ, which characterizes the geometry of the two-droplet system, can vary in the range (0, 1]. The dimensionless relative velocity $\mathbf{v} = \mathbf{V}_{12}/V_{12}^{(0)}$ can be expressed as $\mathbf{v} = v_r\hat{\mathbf{e}}_r + v_\theta\hat{\mathbf{e}}_\theta + v_\phi\hat{\mathbf{e}}_\phi$, where $\hat{\mathbf{e}}_r$, $\hat{\mathbf{e}}_\theta$, and $\hat{\mathbf{e}}_\phi$ are the unit vectors in the r, θ, and ϕ directions, respectively. The components of this velocity are given by

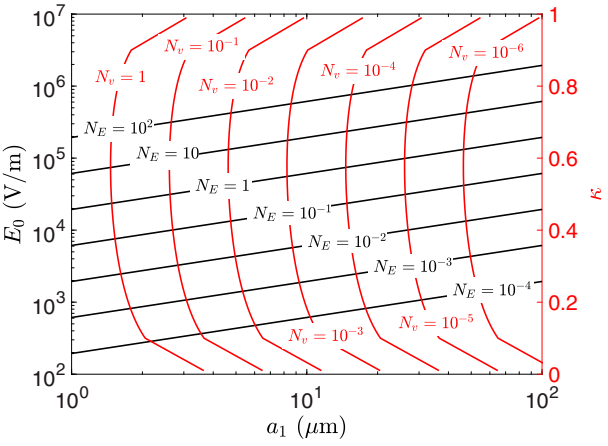

FIG. 2. Typical sizes of droplets and electric fields in clouds. The black and red lines correspond to constant N_E and N_v, respectively.

$$v_r = \frac{dr}{dt} = -L\cos\theta - N_E G\left(\frac{\kappa}{1-\kappa}\right)[F_1\cos^2(\theta-\eta) + F_2\sin^2(\theta-\eta)] - N_v G\frac{d\Phi_{\mathrm{vdW}}}{dr}, \quad (5)$$

$$v_\theta = r\frac{d\theta}{dt} = M\sin\theta + N_E H\left(\frac{\kappa}{1-\kappa}\right)F_8\sin 2(\theta-\eta), \quad (6)$$

$$v_\phi = 0, \quad (7)$$

where N_E and N_v are dimensionless quantities that capture the strength of electric field–induced and van der Waals forces, respectively, compared to gravity:

$$N_E = \frac{3\epsilon_0 E_0^2}{(\rho_p - \rho_f)a_1 g}, \quad (8)$$

$$N_v = \frac{3A_H}{2\pi\kappa(1-\kappa^2)(\rho_p - \rho_f)g a_1^4}. \quad (9)$$

In this problem, N_E primarily depends on the strength of the electric field. We intentionally excluded the size ratio term from the definition of N_E to ensure that the dependence of the collision dynamics on N_E directly correlates with its dependence on E_0. The parameter N_v depends on the size ratio, and this definition is consistent with the earlier works that studied the effect of the van der Waals force on the collisions of droplets settling under gravity. In Fig. 2, we present typical sizes of cloud droplets and electric fields in clouds, along with estimates of the parameters N_E and N_v shown using black and red contours.

b. *Expressions for the collision rate and efficiency*

The collision rate is defined as the rate at which droplets with radii a_1 and a_2 and number densities n_1 and n_2 collide

with each other per unit volume. Mathematically, the collision rate K_{12} is equal to the flux of droplets into the collision sphere of nondimensional radius $r = 2$ and can be expressed in terms of the pair-distribution function $P(r)$ and the droplet relative velocity $\mathbf{v}$ by

$$K_{12} = -n_1 n_2 V_{12}^{(0)} (a^*)^2 \int_{(r=2)\,\&(\mathbf{v}\cdot\mathbf{n}<0)} (\mathbf{v}\cdot\mathbf{n}) P dA, \tag{10}$$

where $\mathbf{n}$ is the outward unit normal at the collision sphere. The condition $\mathbf{v}\cdot\mathbf{n} < 0$ in Eq. (10) implies that the radial relative velocity must be inward at all separations for two droplets coming into contact. For a dilute system like clouds, the pair-distribution function is governed by the quasi-steady Fokker–Planck equation for the region of space outside the collision sphere:

$$\nabla\cdot(P\mathbf{v}) = 0. \tag{11}$$

The uncorrelated motion of the droplets in the far field defines the boundary condition: $P \to 1$ as $r \to \infty$. For the calculation purpose, we take $r = r_\infty$, which is large but finite.

For negligible thermal fluctuations (i.e., Pe $\gg 1$), the relative motion between two droplets induced by gravity and an external electric field is deterministic, and therefore, we can find the collision rate using the trajectory analysis. Using Eq. (11) and the divergence theorem, the integral in Eq. (10) can be taken over the surface that encloses the volume occupied by all trajectories that originate at $r = r_\infty$ and terminate at $r = 2$. Thus, the flux through the cross section A_c of this volume at $r = r_\infty$ defines the collision rate. We call A_c the upstream interception area. At large separations, the electric field–induced and van der Waals forces become insignificant, and gravity solely drives the relative motion between two unequal-sized droplets. Now, at $r = r_\infty$, the pair-distribution function $P = 1$ and $\mathbf{v}\cdot\mathbf{n}' = -1$, where $\mathbf{n}'$ is the unit outward normal vector at the area element of A_c. Therefore, the expression for the collision rate becomes

$$\begin{aligned} K_{12} &= -n_1 n_2 V_{12}^{(0)} (a^*)^2 \int_{A_c} (\mathbf{v}\cdot\mathbf{n}')|_{r_\infty} P dA \\ &= \frac{1}{4} n_1 n_2 V_{12}^{(0)} (a_1 + a_2)^2 \pi \left(\frac{\overline{y}_{c+}^2}{2} + \frac{\overline{y}_{c-}^2}{2} \right), \end{aligned} \tag{12}$$

where $\overline{y}_{c\pm} = y_{c\pm}/a^*$ (with y_{c+} and y_{c-} being the dimensional critical impact parameters for the positive and negative sides of the y axis, respectively, as illustrated schematically in Fig. 1b) are the dimensionless critical impact parameters which define the nondimensional radii of the upstream collisional semicircles at $r = r_\infty$. In other words, these critical impact parameters are the largest possible horizontal distances from the gravity axis at the far field for which two widely separated droplets can still collide. The relative trajectory of the droplets in this scenario is referred to as the limiting colliding trajectory.

The collision rate without any interactions is given by the classical Smoluchowski model (Smoluchowski 1918), where $y_{c+} = y_{c-} = a_1 + a_2$ (i.e., $\overline{y}_{c+} = \overline{y}_{c-} = 2$) (see Fig. 1b). Thus, the expression for the ideal collision rate K_{12}^0 becomes

$$\begin{aligned} K_{12}^0 &= n_1 n_2 V_{12}^{(0)} \pi (a_1 + a_2)^2 \\ &= n_1 n_2 \frac{2(\rho_p - \rho_f)(a_1^2 - a_2^2) g}{9\mu_f} \pi (a_1 + a_2)^2. \end{aligned} \tag{13}$$

The collision efficiency, denoted by E_{12}, is defined as the ratio of K_{12} to K_{12}^0:

$$E_{12} = \frac{K_{12}}{K_{12}^0} = \frac{1}{4}\left(\frac{\overline{y}_{c+}^2}{2} + \frac{\overline{y}_{c-}^2}{2} \right). \tag{14}$$

The droplet pair collides when the initial $\overline{y}$ values at the far field belong to $[\overline{y}_{c-}, \overline{y}_{c+}]$. Therefore, the problem now becomes one of determining the dimensionless critical impact parameters $\overline{y}_{c\pm}$. In the subsequent section, we will describe the numerical methodology employed to find $\overline{y}_{c\pm}$ through a detailed analysis of the relative trajectories of a pair of droplets.

It is important to note that Davis (1984) derived a closed-form analytical expression for the collision efficiency in the absence of nonhydrodynamic forces (i.e., when $N_E = N_v = 0$). The expression is given by

$$E_{12} = \exp\left(-2 \int_2^\infty \frac{M - L}{rL} dr \right). \tag{15}$$

However, with continuum lubrication, the integrand behaves as $O[(r-2)^{-1}]$, causing the integral to diverge and consequently leading to the vanishing of E_{12}. This reiterates our earlier point: In the absence of any attractive force such as van der Waals interactions, collisions do not occur under continuum lubrication theory. In contrast, when noncontinuum effects are taken into account, the integrand exhibits an integrable singularity. For small Knudsen numbers, the asymptotic form of the collision efficiency scales as $\mathrm{Kn}^{q_1}/[\log(1/\mathrm{Kn})]^{q_2}$, where q_1 and q_2 are the positive constants that depend on the size ratio (see Dhanasekaran et al. 2021a).

3. Numerical method

Since the relative velocity between the droplets is independent of the azimuthal coordinate ϕ, we can restrict our analysis to a representative $r\sin\theta$–$r\cos\theta$ plane. To find the relative trajectories of the droplets, we integrate the following dimensionless trajectory equation:

$$\frac{d\theta}{dr} = \frac{v_\theta}{r v_r}. \tag{16}$$

This equation describes the relative trajectory of a pair of droplets, influenced by the combined effects of gravity, hydrodynamic interactions, electric field–induced forces, and van der Waals forces. Depending on the computational requirements, we sometimes solve for $r(\theta)$ from the rearranged form $dr/d\theta = (rv_r)/v_\theta$ instead of solving for $\theta(r)$ from Eq. (16).

Colliding trajectories refer to the paths traced by the centers of evolving satellite droplets that start far upstream and ultimately reach the collision surface. In the far field, these colliding trajectories define the upstream interception area.

The computational cost of determining these colliding trajectories can become prohibitively expensive if we choose initial conditions on a plane located far upstream and perpendicular to gravity, as most trajectories starting from that plane would never reach the collision sphere. To mitigate this computational challenge, we exploit the quasi-steady nature of the relative trajectory equation. We employ backward integrations of the relative trajectory equation using a fourth-order Runge–Kutta method, with initial conditions set on the collision sphere ($r = 2$). However, at exactly $r = 2$, $v_r = 0$, as the hydrodynamic mobilities L and G are both zero at $r = 2$. To avoid this issue, we set our initial conditions on a sphere with a radius of $2 + \delta$, where δ is a small separation from the collision surface. We will show converged results with reasonable computational effort when $\delta = 10^{-6}$. As stated in Eq. (10), the radial relative velocity must be inward at the collision sphere for a colliding trajectory. Consequently, we further optimize our computational approach by selecting only those points on the collision sphere where $v_r < 0$.

After computing colliding trajectories, we identify the limiting colliding trajectories as those exhibiting maximum horizontal shifts from the gravitational axis in the far field. This leads to the determination of the critical impact parameters $\bar{y}_{c\pm}$. We then use $\bar{y}_{c\pm}$ values to calculate the collision efficiency from Eq. (14). This numerical methodology allows us to compute the collision efficiency over a range of values for κ, Kn, η, N_E, and N_v.

4. Results and discussion

To systematically investigate the effects of an external electric field on the relative trajectories and collision efficiency of droplets, we begin our analysis by considering a scenario in which the droplets interact exclusively through hydrodynamic forces and those induced by the electric field (i.e., with a finite N_E), while neglecting van der Waals interactions (i.e., setting $N_v = 0$). We subsequently extend our analysis to include van der Waals forces. Figure 3 illustrates typical limiting colliding trajectories for weak ($N_E \ll 1$) and strong ($N_E \gg 1$) electric fields, under conditions where Kn $= 10^{-2}$, $\kappa = 0.9$, and $\eta = 0$. As expected, when N_E is small, the trajectories closely resemble those observed in pure gravitational sedimentation, with the limiting colliding trajectories reaching the collision sphere at $\theta = \pi/2$ (see Dhanasekaran et al. 2021b). The open and colliding trajectories shown in the background represent a typical trajectory map driven solely by differential sedimentation.

In contrast, at large values of N_E, the attractive force induced by the electric field facilitates surface-to-surface contact between droplets, even when the initial horizontal separation between their centers is significantly greater than in cases with weaker electric fields. Furthermore, the forces and torques imposed by the strong electric field cause the relative trajectories to bend sharply before reaching the collision surface. Since gravity dominates the relative motion at large separations, far-field trajectories remain nearly indistinguishable from the open trajectories (represented by the blue line in Fig. 3) that would occur in the absence of an electric field. However, when the electric field entirely governs the dynamics, the relative trajectories originate

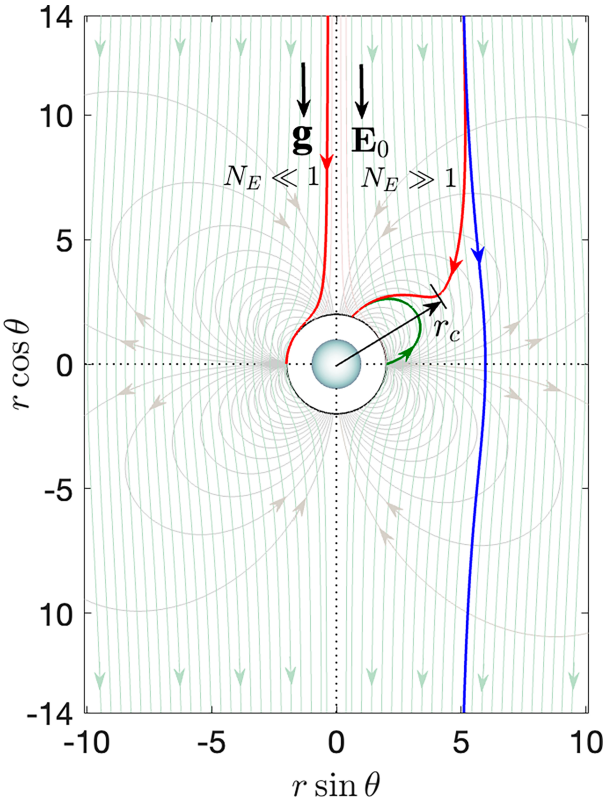

FIG. 3. Typical limiting colliding trajectories (continuous red lines) for weak ($N_E \ll 1$) and strong ($N_E \gg 1$) electric field. The blue and green lines indicate the open and loop trajectories due to differential sedimentation and a vertical electric field only. A complete map of trajectories for gravity alone (open and colliding) and a vertical electric field alone (loop trajectories) are provided in the background for reference. Here, r_c indicates the separation distance where the effects of gravity and the electric field–induced forces are comparable. The sphere at the center represents the test droplet, and the thin black circle represents the projection of the collision sphere. Representative arrows on the trajectories indicate their directions.

and terminate on the collision sphere, forming what we call loop trajectories. These loop trajectories are comprehensively analyzed in Thiruvenkadam et al. (2023). A set of these loop trajectories, shown as light black lines in Fig. 3, represents cases where a vertical electric field solely dictates the relative motion of the droplets. In the near field, electric field–induced forces and torques dominate the interactions, leading to the merging of the limiting colliding trajectory with a loop trajectory before reaching the collision surface. We identify a characteristic radial location, denoted as r_c, where the effects of gravity and the electric field become comparable, resulting in a sharp bend in the trajectory. Later in this section, we will use the scaling of r_c with N_E to predict the scaling behavior of collision efficiency in the strong-field regime.

A detailed examination of how relative trajectory topologies evolve with increasing electric field strength is essential for accurately characterizing the collision dynamics. Figures 4–6 illustrate the representative pair trajectories for three different electric field orientations: $\eta = 0$, $\eta = \pi/4$, and $\eta = \pi/2$,

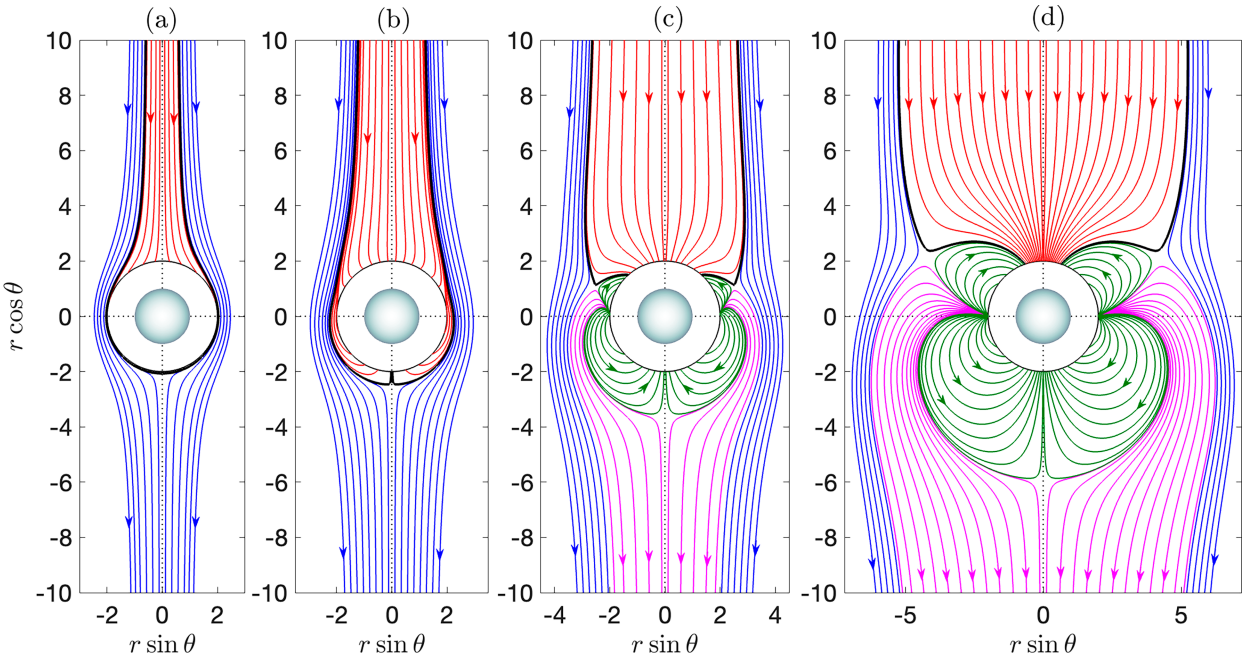

FIG. 4. Pair trajectories of two differentially sedimenting droplets with a vertical electric field ($\eta = 0$) for noncontinuum hydrodynamic interactions ($\mathrm{Kn} = 10^{-2}$) when $\kappa = 0.5$, $N_v = 0$, and (a) $N_E = 10^{-1}$, (b) $N_E = 1$, (c) $N_E = 10$, and (d) $N_E = 10^2$. The blue, green, red, and thick black lines are open, loop, colliding, and limiting colliding trajectories. Pink lines are a separate class of trajectory that starts from two specific locations on the collision surface and goes to infinity.

respectively, while keeping all other parameters constant. Specifically, we set $\kappa = 0.5$, $\mathrm{Kn} = 10^{-2}$, and $N_v = 0$ and examine the relative trajectories for four different electric field strengths: $N_E = 10^{-1}$, $N_E = 1$, $N_E = 10$, and $N_E = 10^2$, shown in panels a–d, respectively.

For small N_E, the relative trajectories resemble those observed in the absence of an electric field, consisting solely of open and colliding trajectories. However, as N_E increases, loop trajectories—characteristic of motion governed primarily by the electric field—begin to emerge. The locations on the collision surface where these loop trajectories originate depend on the angle η between gravity and the electric field. We find that loop trajectories initiate at $\theta = \eta + (\pi/2)$ and $\theta = \eta + (3\pi/2)$ and terminate at different locations on the collision sphere.

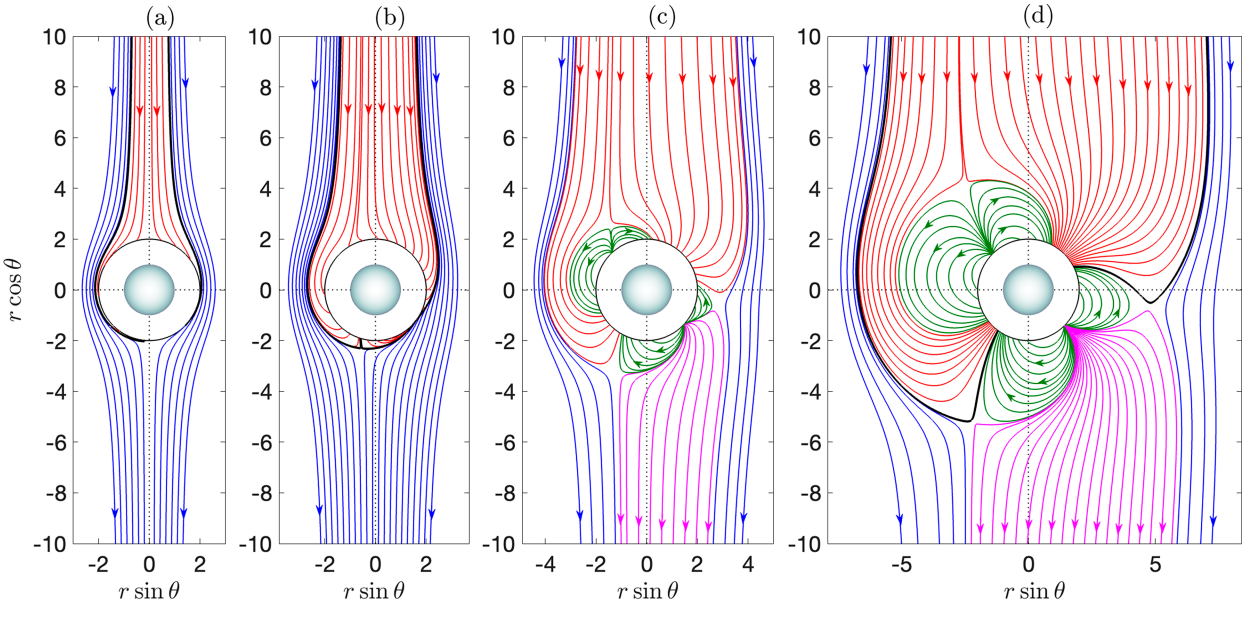

FIG. 5. As in Fig. 4, except $\eta = \pi/4$.

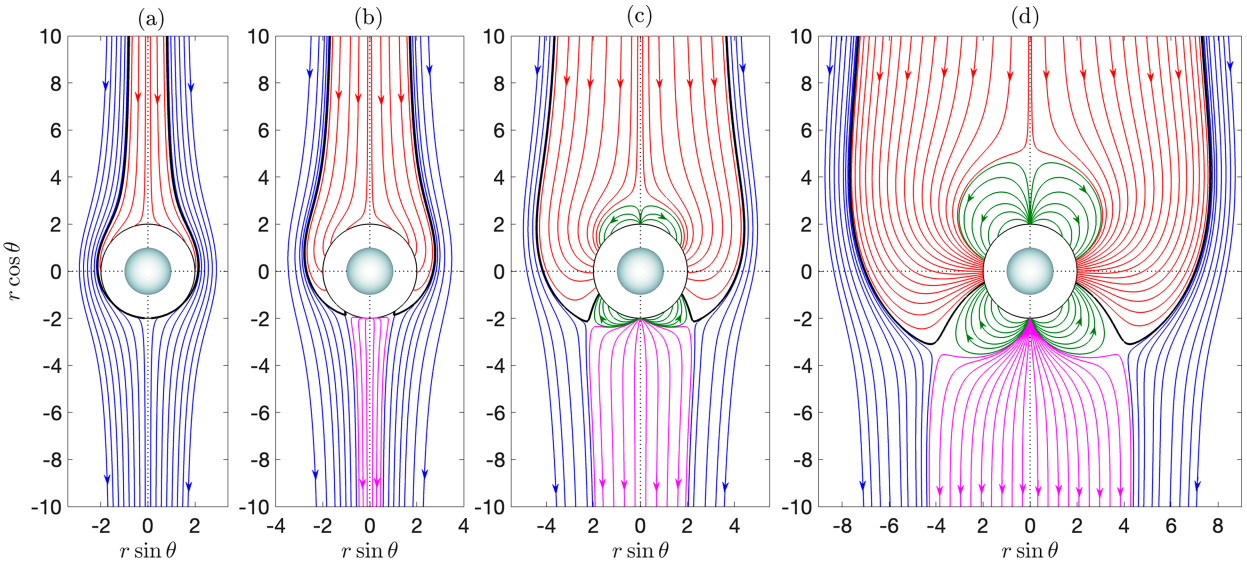

FIG. 6. As in Fig. 4, except $\eta = \pi/2$.

These starting locations act as unstable fixed points in the system, but not all trajectories originating from these points form loops. Interestingly, some trajectories (shown in pink) diverge to infinity instead, and the volume occupied by these trajectories increases with increasing N_E.

As N_E grows asymptotically large, all colliding trajectories converge toward impact locations centered around $\theta = \eta$ and $\theta = \eta + \pi$. The limiting colliding trajectories serve as separatrices, depicted as thick black lines in Figs. 4–6. These separatrices distinguish open trajectories from colliding trajectories for small to moderate N_E. However, at larger N_E, they instead delineate colliding trajectories from open trajectories in the far field and from loop trajectories in the near field. Though not explicitly shown in the figures, for sufficiently large N_E, the limiting colliding trajectories and outermost pink trajectories intersect at points of maximum curvature for both curves. These intersections correspond to saddle points in the system, whose positions are strongly influenced by η.

Despite this dependence on η, the critical impact parameters consistently increase with increasing electric field strength. Additionally, the trajectories exhibit asymmetry about the gravity axis, except in cases where the electric field is oriented either purely vertically or horizontally. Importantly, the fundamental trajectory topology for strong electric fields remains unchanged even when droplets interact through pure continuum hydrodynamics. This is because the electric field–induced forces can overcome continuum lubrication resistance, allowing droplets to make surface-to-surface contact within a finite time.

We now investigate the effect of the electric field on collision efficiency, which we can determine from the trajectory analysis presented previously. The rest of this section will explore how collision efficiency varies with the different parameters involved in the problem. Figure 7a illustrates the variation of collision efficiency with the relative strength of electric field–induced force and gravity (N_E) for $\kappa = 0.5$, $\mathrm{Kn} = 10^{-2}$, and $N_v = 0$ when the angles between the electric field and gravity are $\eta = 0$, $\pi/6$, $\pi/4$, $\pi/3$, and $\pi/2$. In the

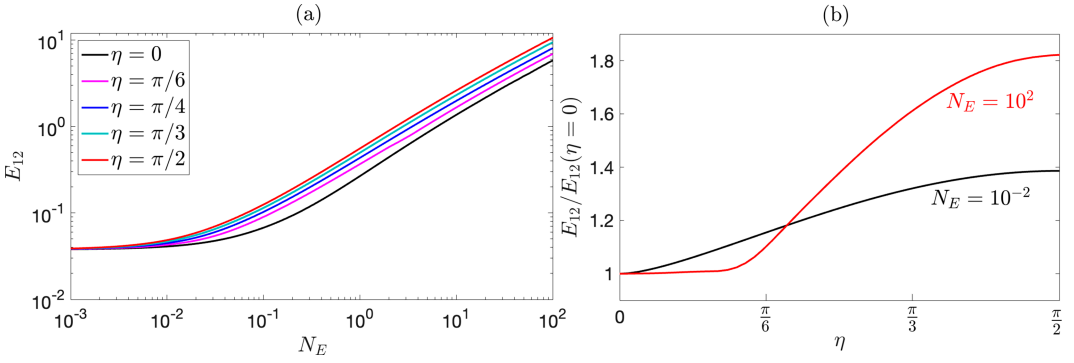

FIG. 7. (a) Collision efficiency as a function of relative strength of electric field–induced forces and gravity N_E for different angles between the electric field and gravity η when $\kappa = 0.5$, $\mathrm{Kn} = 10^{-2}$, and $N_v = 0$. (b) Collision efficiencies scaled with their values for $\eta = 0$ as a function of η for $N_E = 10^{-2}, 10^2$ when $\kappa = 0.8$, $\mathrm{Kn} = 10^{-2}$, and $N_v = 0$.

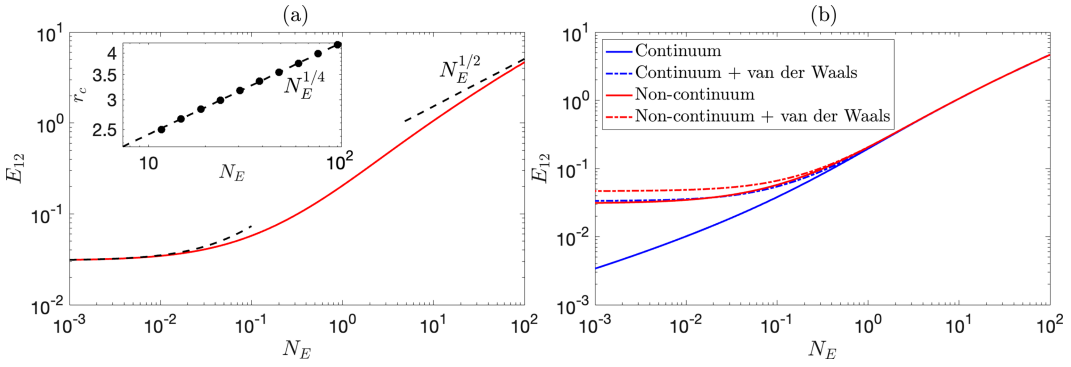

FIG. 8. (a) Collision efficiency as a function of N_E with asymptotics for small and large N_E limits when $\kappa = 0.9$, $\mathrm{Kn} = 10^{-2}$, $N_v = 0$, and $\eta = 0$. The black dashed lines indicate the asymptotics. The inset shows the behavior of r_c for $N_E \gg 1$. (b) Variation in collision efficiency with N_E for different collision-inducing mechanisms. All parameters are the same as in (a) except for the cases with the van der Waals force where $N_L = 500$ and $N_v = 10^{-3}$.

gravity-dominated regime (i.e., $N_E \ll 1$), all the curves tend to merge since the noncontinuum lubrication interactions drive the collision mechanisms across all cases in a similar way for a given κ and Kn. The collision efficiency increases monotonically with the increase in the electric field-induced force, and E_{12} grows according to a power law for large N_E. We find that the collision efficiency is higher for a higher η. To explicitly show the dependency of collision efficiency on η, we plot collision efficiency scaled by its value for $\eta = 0$ as a function of η for weak ($N_E = 10^{-2}$) and strong ($N_E = 10^{2}$) electric fields when $\kappa = 0.8$, $\mathrm{Kn} = 10^{-2}$, and $N_v = 0$ (see Fig. 7b). In both cases, the scaled collision efficiency increases as η increases from 0 to $\pi/2$. However, there is a subtle difference in how they increase with η. For a high N_E value (i.e., $N_E = 10^2$), the collision efficiency remains almost constant up to a certain value of η and then increases monotonically with increasing η. This behavior has a correlation with the corresponding pair trajectory map in terms of the locations of the saddle points. We observe that both the saddle points lie above or below the $r\sin\theta = 0$ line for η values below or above this certain value. On the other hand, for a small value of N_E (i.e., $N_E = 10^{-2}$), the collision efficiency increases monotonically as η increases, and this behavior corresponds to a small perturbation effect due to a weak electric field on the collision efficiency of two sedimenting droplets with noncontinuum lubrication interactions. In the appendix, we derive the analytical expression for the collision efficiency up to $O(N_E)$ using a regular perturbation expansion. Figure 8a illustrates the validity of the asymptotic calculation in the small N_E limit for a vertical electric field when $\kappa = 0.9$, $\mathrm{Kn} = 10^{-2}$, and $N_v = 0$. On the other hand, to predict the power-law behavior for large N_E, we present the following scaling argument. The first and second terms in the radial relative velocity equation (5) are comparable at r_c, which typically happens to be a large separation. Now, L, $G \to 1$ and F_1, $F_2 \to 1/r^4$ in the far field. Thus, from Eq. (5), we have $r_c \sim N_E^{1/4}$ and $E_{12} \sim r_c^2 \sim N_E^{1/2}$. This scaling relation is valid irrespective of the value of η. Figure 7a, where lines are parallel for large N_E, confirms this argument. We fit the data for large N_E shown in the inset of Fig. 8a, which confirms our scaling argument. In the presence of strong electric fields, electrostatic forces become the dominant driver of collisions such that the overall scaling of collision efficiency remains unaffected across modeling choices, such as the inclusion of full continuum hydrodynamics and van der Waals interactions (see Fig. 8b). The continuous blue line in Fig. 8b represents the collision efficiency when the droplet pair interacts via full continuum hydrodynamics. In this case, E_{12} decreases rapidly with decreasing N_E, and theoretically, it will approach zero for $N_E \to 0$. However, in the presence of van der Waals force, the collision efficiency asymptotically approaches a finite value as $N_E \to 0$, even when droplets interact via continuum hydrodynamics (the dash–dotted blue line in Fig. 8b). This behavior arises because van der Waals forces drive the collision dynamics in the gravity-dominated regime when droplets interact through full continuum hydrodynamics. As expected, for small to moderate values of N_E, the collision efficiency due to noncontinuum hydrodynamics plus van der Waals interactions (the dash–dotted red line in Fig. 8b) becomes higher than that due to noncontinuum hydrodynamics alone.

We will now demonstrate how variations in the strength of noncontinuum lubrication effects modify collision dynamics. Figure 9a shows the collision efficiency as a function of Knudsen number for values of $N_E = 10^{-1}$ and 1, under the conditions where $\kappa = 0.5$, $N_L = 250$, $N_v = 10^{-2}$, and $\eta = 0$. We compare these findings with those of Dhanasekaran et al. (2021b), who calculated the collision efficiency of two sedimenting droplets by considering noncontinuum hydrodynamics, including both scenarios with and without van der Waals forces. The black line in Fig. 9a represents the collision efficiency resulting solely from noncontinuum effects, as computed by Dhanasekaran et al. (2021b) through the evaluation of the integral in Eq. (15) for various values of Kn. As Kn decreases, the relative thickness of the noncontinuum lubrication layer also decreases, causing the collision efficiency attributed to noncontinuum lubrication effects alone to decrease monotonically, approaching zero in the limit as Kn approaches zero. The collision efficiency due to the combined effects of noncontinuum hydrodynamics and van der Waals forces also exhibits a decrease with diminishing Kn (illustrated by the pink line in Fig. 9a). However, in this case, E_{12} asymptotically approaches a finite value as Kn approaches zero because the van der Waals attraction forces

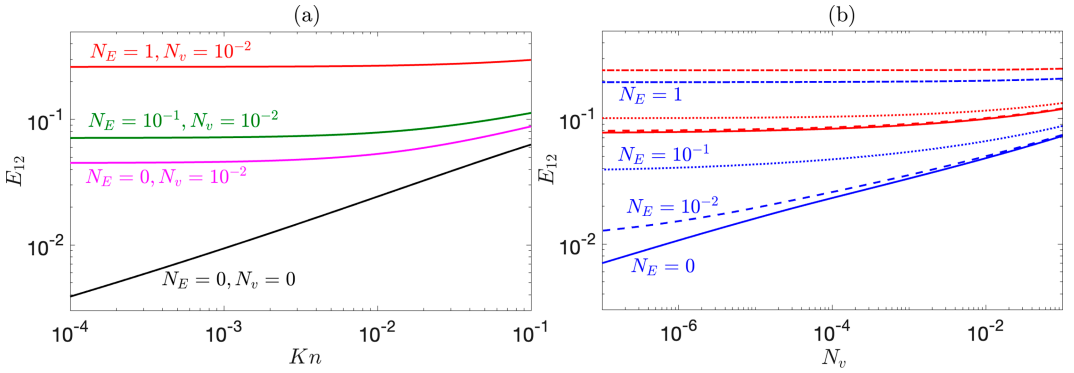

FIG. 9. (a) Collision efficiency as a function of Kn for noncontinuum hydrodynamics alone (continuous black line), noncontinuum hydrodynamics plus van der Waals forces (continuous pink line), and noncontinuum hydrodynamics plus van der Waals forces and electric field–induced forces with $N_E = 10^{-1}$ and 1.0 when $\kappa = 0.5$, $N_L = 250$, $N_v = 10^{-2}$, and $\eta = 0$. (b) Collision efficiency as a function of N_v for continuum (blue lines) and noncontinuum (Kn $= 10^{-1}$; red lines) lubrication interactions when $\kappa = 0.9$, $N_L = 500$, $\eta = 0$, and $N_E = 0, 10^{-2}, 10^{-1}, 1.0$.

dominate the asymptotic behavior for small Kn, while the noncontinuum effects become negligible. As expected, including electric field–induced forces, alongside noncontinuum and van der Waals interactions, increases the collision efficiencies compared to cases without an external electric field. When the electric field strength is relatively weak (e.g., $N_E = 10^{-1}$), the dependence of E_{12} on Kn closely resembles the behavior of collision efficiency driven by the combined effects of noncontinuum hydrodynamics and van der Waals forces. However, under strong electric field strength conditions, the electric field–induced forces dominate over the combined effects of noncontinuum lubrication interactions and van der Waals forces, rendering the collision efficiency independent of Kn. Consequently, the Kn versus E_{12} curve, represented by the red line ($N_E = 1$) in Fig. 9a, becomes a straight line parallel to the Kn axis.

To investigate the behavior of collision efficiency under varying strengths of the van der Waals force, we plot E_{12} for N_v ranging from 10^{-7} (indicating a weak van der Waals force) to 10^{-1} (indicating a strong van der Waals force) (see Fig. 9b). The parameter values used in this analysis are $\kappa = 0.9$, Kn $= 10^{-1}$, $N_L = 500$, and $N_E = 0, 10^{-2}, 10^{-1}, 1$. In this figure, we also compare the results to their continuum counterparts. As anticipated, the collision efficiency E_{12} decreases with the diminishing strength of the van der Waals force. This decrease in E_{12} becomes particularly significant when droplets interact via continuum hydrodynamics and the electric field strength is zero ($N_E = 0$) or low ($N_E = 10^{-2}$). However, when we consider noncontinuum lubrication interactions, E_{12} decreases at a relatively slow rate and asymptotically approaches values corresponding to collision efficiency due to noncontinuum effects alone at $N_E = 0$ and the combined influence of noncontinuum effects and electric field–induced forces at $N_E = 10^{-2}$ and 10^{-1}. Interestingly, when the imposed electric field strength is high (for instance, at $N_E = 1$), the collision efficiency becomes independent of the van der Waals force, as the electric field–induced forces dominate all other factors contributing to a finite collision rate.

To examine how size differences between cloud droplets influence their dynamics under the combined effects of noncontinuum hydrodynamics, van der Waals forces, and electric field–induced forces, we plot the collision efficiency as a function of N_E for $\kappa = 0.3, 0.6, 0.9$ and $\eta = 0, \pi/2$ with Kn $= 10^{-2}$, $N_L = 500$, and $N_v = 10^{-3}$ (see Fig. 10). The collision efficiency trends for each size ratio are consistent with those discussed earlier. In the gravity-dominated regime, collision efficiency decreases as κ decreases because the smaller droplet tends to follow the flow streamlines and move around the larger droplet. As a result, collisions occur only if the smaller droplet follows a streamline very close to the larger one. Additionally, as the size ratio decreases, electric field–induced forces weaken, further reducing the collision efficiency across all values of N_E.

Our discussion thus far has focused on how collision efficiency varies with different nondimensional quantities relevant to the problem. Now, we will present some results considering the property values of water droplets under typical cloud conditions when the radius of the larger droplet $a_1 = 10$ μm. Typical values for droplet density ρ_p, air density ρ_f, the dynamic viscosity of air μ_f, and electric field strength E_0 are provided in section 1. The mean free path of air increases with altitude, and for warm cumulus clouds, $\lambda_0 \sim 0.1$ μm (see Wallace and Hobbs 2006). Consequently, we express the Knudsen number as a function of size ratio as Kn $= 0.02/(1 + \kappa)$. For water droplets in air, the Hamaker constant is $A_H \approx 3.7 \times 10^{-20}$ J (see Friedlander 2000). Therefore, we express the parameters N_L and N_v in terms of κ as follows: $N_L = 6.28 \times 10^2\,(1 + \kappa)$ and $N_v = 1.77 \times 10^{-4}/[\kappa(1 - \kappa^2)]$. The parameter N_E defined above does not depend on the size ratio, and it varies with the strength of the electric field according to the relation $N_E = 2.66 \times 10^{-10} E_0^2$. For a given κ and E_0, we determine the required dimensionless parameters (Kn, N_L, N_v, and N_E) from these relations and then calculate the collision efficiency. Figure 11 shows how collision efficiency increases as the strength of the vertical or horizontal electric field increases when $a_2 = 3$ μm (i.e., $\kappa = 0.3$ indicating droplets with significantly different in size) and $a_2 = 9$ μm (i.e., $\kappa = 0.9$ indicating droplets with almost equal in size). For electric field strengths E_0 up to a few thousand volts per meter, E_{12} increases very slowly,

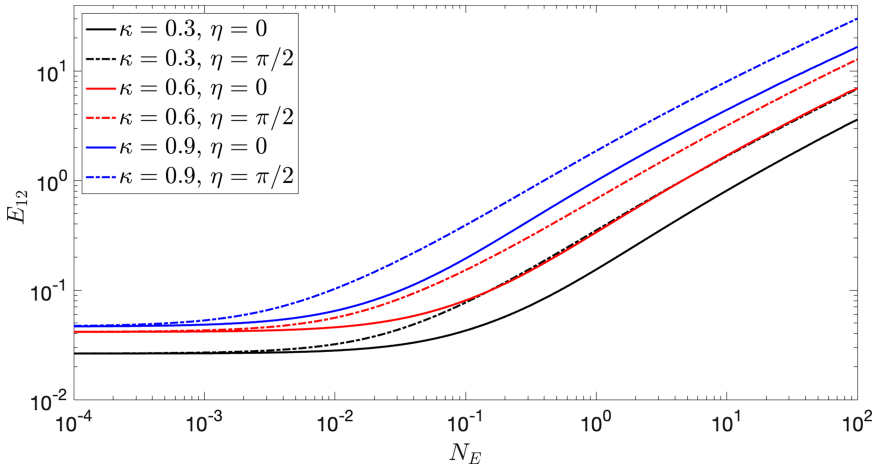

FIG. 10. Collision efficiency as a function of N_E for Kn $= 10^{-2}$, $N_L = 500$, and $N_v = 10^{-3}$ when $\kappa = 0.3$, 0.6, and 0.9, and $\eta = 0$, $\pi/2$.

suggesting that the contribution of the fair-weather electric field in droplet–droplet collisions is insignificant. The dashed lines in Fig. 11 represent the results calculated from the analytical expression [Eq. (A12)] for the weak electric fields. These results also demonstrate that the asymptotic expression accurately predicts the collision efficiency influenced by the fair-weather atmospheric electric field. The enhancement in collision efficiency becomes rapid when the electric field strengths exceed 10^4 V m^{-1}, typical in strongly electrified clouds. More precisely, for strong electric fields, $E_{12} \sim N_E^{1/2} \sim E_0$ since N_E varies with the square of the strength of the electric field.

Finally, we estimate how collision efficiency varies with the size ratio κ of cloud droplets in the presence of vertical and horizontal electric fields with strengths of 5×10^4 and 3×10^5 V m^{-1}, along with the influence of van der Waals forces (see Fig. 12). In this analysis, we keep $a_1 = 10$ μm, making the relation $N_E = 2.66 \times 10^{-10} E_0^2$ and the relations of Kn, N_L, and N_v with κ mentioned above remain applicable. We find that collision efficiency increases with the size ratio as the electric field-induced forces become stronger with a higher size ratio. Notably, for a specific pair of droplets, the collision efficiency increases by an order of magnitude when the electric field strength increases from 5×10^4 to 3×10^5 V m^{-1}. Our findings also suggest that a horizontal electric field is more effective than a vertical one in promoting collisions between droplets. As discussed in section 1, gravity-induced collisions due to continuum and noncontinuum hydrodynamics, as well as van der Waals forces, have received comprehensive treatment in the existing literature (refer to Davis 1984; Dhanasekaran et al. 2021b). The comparison of these results—represented by the three bottom lines in Fig. 12—with our current findings demonstrates that an external electric field consistently enhances collision efficiency.

5. Summary and conclusions

We have quantified the influence of an external electric field on the collision rate of uncharged cloud droplets settling under gravity in a quiescent atmosphere. Our study builds upon recent analytical formulations for electric field–induced forces at close separations, demonstrating that these forces can overcome lubrication resistance and enable surface-to-surface contact within a

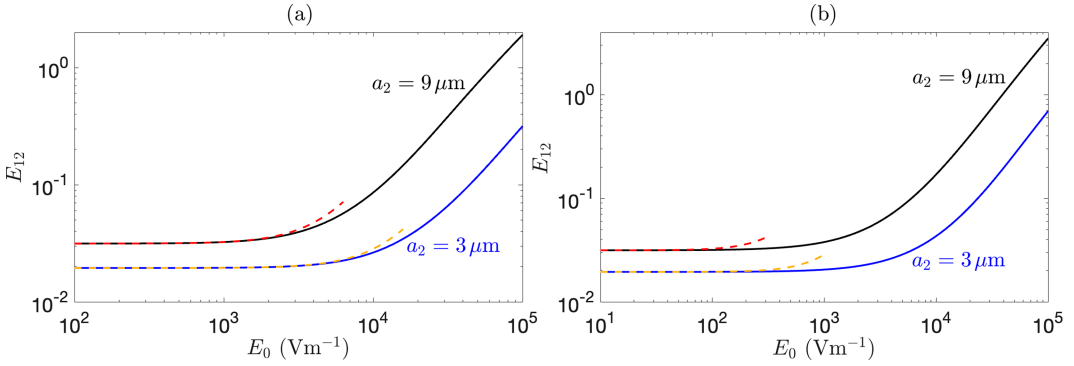

FIG. 11. Collision efficiency as a function of strength of the external electric field for a pair of water droplets in air with $a_1 = 10$ μm and $a_2 = 3$, 9 μm when van der Waals forces are absent, and the electric field acts in the (a) vertical direction and (b) horizontal direction. Dashed lines are from the asymptotic expression of collision efficiency for the weak electric field.

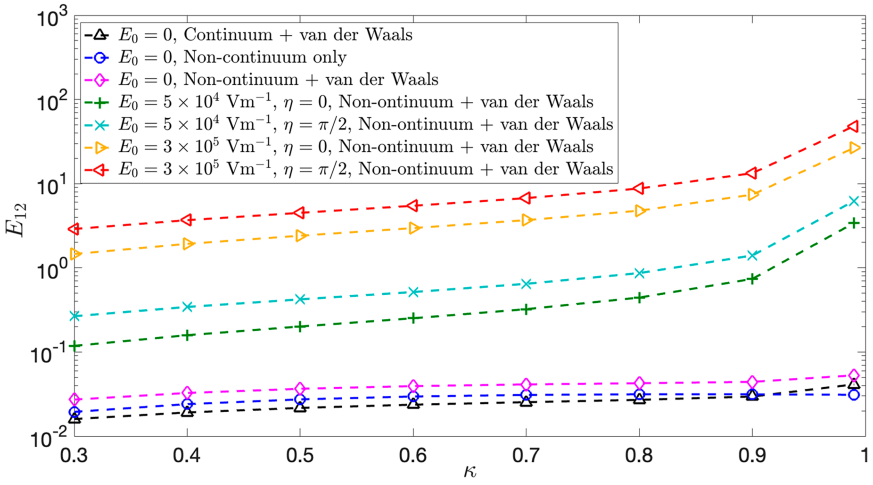

FIG. 12. Collision efficiency as a function of size ratio for water droplets in air with $a_1 = 10$ μm, vertical ($\eta = 0$) and horizontal ($\eta = \pi/2$) electric field strengths $E_0 = 5 \times 10^4$, 3×10^5 V m^{-1} when noncontinuum effects, van der Waals interactions, and electric field–induced forces act together. We included the results from previous studies (see Davis 1984; Dhanasekaran et al. 2021b) that predicted collision efficiencies without an external electric field to compare our findings.

finite time. Additionally, we incorporated noncontinuum hydrodynamic effects, which are essential for accurately modeling cloud droplet collisions.

The pair trajectory maps presented in Figs. 4–6 illustrate how electric field–induced forces modify pair trajectories that would exist in purely gravity-driven interactions. We found that collisions occur even when droplets interact via continuum hydrodynamics. In section 4, we have presented how the collision efficiency varies with droplet size ratio (κ), the Knudsen number (Kn), the angle between electric field and gravity axis (η), the relative strength of electric field–induced forces and gravity (N_E), and the relative strength of van der Waals force and gravity (N_v). Our findings quantitatively demonstrated how increasing these parameters leads to enhanced collision efficiency. However, strong electric fields always dominate the dynamics and significantly enhance collision efficiency.

While our analysis provides new insights, it does not account for the effects of droplet inertia, which can significantly influence the collision rate for larger droplet pairs. Moreover, cloud droplets often carry surface charges, making it necessary to consider both external electric field effects and direct electrostatic interactions between charged droplets. Our recent study (Patra et al. 2023) on like-charged settling droplets (neglecting inertia) has shown a nonmonotonic relationship between surface charge and collision efficiency: an initial increase due to near-field attraction, followed by a sharp decrease due to far-field repulsion. A natural extension of our work would be to incorporate exact hydrodynamic and electrostatic forces into the collision rate calculations for sedimenting inertial droplets, which may reveal further complexities in droplet interactions.

Another crucial factor not addressed in this study is atmospheric turbulence, which plays a key role in the growth of cloud droplets and the initiation of rainfall (Shaw 2003). In the size-gap regime, turbulence enhances collision rates through (i) increased radial relative velocities between droplet pairs (Saffman and Turner 1956; Falkovich and Pumir 2007) and (ii) preferential concentration of inertial droplets in straining regions of the flow (Sundaram and Collins 1997; Chun et al. 2005). Additionally, the velocity perturbations induced by droplet motion further influence collision rates under realistic conditions (Pinsky et al. 2007). Recent direct numerical simulations coupled with Lagrangian particle tracking (Chen et al. 2018; Michel et al. 2023) have demonstrated that turbulence and droplet aerodynamic interactions significantly broaden the droplet size distribution. A recent study by Patra et al. (2025) on droplets in a background linear flow with an electric field reported the results consistent with the present study's findings for pure gravitational settling—showing that electric fields can significantly enhance droplet collisions. However, there are currently no theoretical predictions for collision efficiencies of inertial droplets under the combined effects of turbulence, gravity, and an external electric field. Future studies should aim to incorporate these factors into collision rate calculations, including a rigorous treatment of short-range electric field–induced forces.

Our discussion has focused exclusively on warm clouds, where droplet collisions govern the formation of raindrops. However, mixed-phase clouds contain both supercooled droplets and ice crystals, and their interactions play a fundamental role in precipitation formation. For instance, snow aggregates form through collisions between ice crystals, while graupel growth occurs via rimming—when settling ice crystals collide with supercooled droplets under turbulent conditions (Pruppacher and Klett 1997; Wang 2013). While spherical droplet collisions are well understood, ice crystal collisions remain less explored due to their anisotropic shapes and variable settling orientations. Recent studies (Jucha et al. 2018; Sheikh et al. 2022) have examined turbulence and gravitational effects on ice crystal collisions, while

others have explored collisions between ice crystals and supercooled droplets (Naso et al. 2018; Jost et al. 2019; Sheikh et al. 2024). However, these studies rely on the ghost collision approximation, which neglects hydrodynamic and electrostatic interactions between colliding hydrometeors. Given that electrostatic forces can become significant at close distances, they may substantially influence ice crystal collision outcomes. Recent work by Joshi and Roy (2025) has quantified electrostatic forces and torques between charged anisotropic particles, showing that electrostatic torques can induce preferential alignment of ice crystals, thereby affecting their interactions. Future research should incorporate these electrostatic effects into collision rate calculations, considering both translational and rotational dynamics to achieve a more comprehensive understanding of hydrometeor interactions due to electric effects.

Acknowledgments. The authors acknowledge the support from IIT Madras for its support of the Centre for Atmospheric and Climate Sciences (CACS) research initiative under the Institute of Eminence framework. P. P. would like to acknowledge the financial support from the Prime Minister's Research Fellows (PMRF) scheme, Ministry of Education, Government of India (Project Number: SB22230184AMPMRF008746). A.R. would like to acknowledge the financial support of SPARC scheme, Ministry of Education, Government of India (Project No. SPARC/2024-2025/ENSU/P3599).

Data availability statement. The data that support the findings of this study are available within the article.

APPENDIX

Analytical Expression for the Collision Efficiency when $N_E \ll 1$ and $N_v = 0$

We can analytically determine the relative trajectories when the applied electric field is weak. Let us assume that the solution for $\theta(r)$ takes the form $\theta(r) = \theta_0(r) + N_E\theta_1(r) + O(N_E^2)$, where θ_0 and θ_1 represent the solutions at $O(1)$ and $O(N_E)$, respectively. In the absence of the van der Waals force ($N_v = 0$), the relative trajectory equations at $O(1)$ and $O(N_E)$, derived from Eq. (16), are as follows:

$$\frac{d\theta_0}{dr} = -\frac{M}{rL}\tan\theta_0, \tag{A1}$$

and

$$\frac{d\theta_1}{dr} + \frac{M\sec^2\theta_0}{rL}\theta_1 = Q(r), \tag{A2}$$

where

$$Q(r) = \frac{GM\sin\theta_0}{rL^2\cos^2\theta_0}C_\kappa[F_1\cos^2(\theta_0 - \eta) + F_2\sin^2(\theta_0 - \eta)] + \frac{H\sec\theta_0}{rL}C_\kappa F_8\sin 2(\eta - \theta_0). \tag{A3}$$

Here, $C_\kappa = \kappa/(1-\kappa)$. We need to find the dimensionless critical impact parameter to calculate the collision efficiency by determining the limiting colliding trajectory. To find the limiting colliding trajectory, we set $v_r = 0$ and then obtain the boundary conditions for Eqs. (A1) and (A2). Thus, the boundary conditions for the $O(1)$ and $O(N_E)$ trajectory equations are as follows:

$$\theta_0(r=2) = \frac{\pi}{2}, \tag{A4}$$

and

$$\theta_1 = \left.\frac{GC_\kappa\{F_1\cos^2[\theta_0(r) - \eta] + F_2\sin^2[\theta_0(r) - \eta]\}}{L\sin\theta_0(r)}\right|_{r=2} = B(\text{let's say}). \tag{A5}$$

The solutions for $\theta_0(r)$ and $\theta_1(r)$ are

$$\theta_0(r) = \sin^{-1}\left\{\exp\left[\int_2^r -\frac{M(r')}{r'L(r')}dr'\right]\right\}, \tag{A6}$$

$$\theta_1(r) = \exp\left[-\int_2^r \frac{M(r')\sec^2\theta_0(r')}{r'L(r')}dr'\right]\left\{B + \int_2^r Q(r')\exp\left[\int_2^{r'}\frac{M(r'')\sec^2\theta_0(r'')}{r''L(r'')}dr''\right]dr'\right\}. \tag{A7}$$

For a weak electric field, the upstream interception area is approximately a circle, and thus, $\bar{y}_{c+} \approx \bar{y}_{c-} = \bar{y}_c$. The dimensionless critical impact parameter can be written as

$$\bar{y}_c = \lim_{r\to\infty} r\sin\theta = \lim_{r\to\infty} r\sin[\theta_0(r) + N_E\theta_1(r)] + O(N_E^2) = \bar{y}_{c0} + N_E\bar{y}_{c1} + O(N_E^2). \tag{A8}$$

In Eq. (A8), $\bar{y}_{c0}$ and $\bar{y}_{c1}$ can be expressed as

$$\bar{y}_{c0} = \lim_{r\to\infty} r\sin\theta_0 = 2\exp\left(-\int_2^\infty \frac{M-L}{rL}dr\right), \tag{A9}$$

$$\bar{y}_{c1} = \lim_{r\to\infty}(r\cos\theta_0)\theta_1 = \bar{y}_{c0}\left[\exp\left(2\int_2^\infty \frac{M}{rL}dr\right) - 1\right]^{1/2}\lim_{r\to\infty}\theta_1(r). \tag{A10}$$

The expression for the collision efficiency in terms of $\bar{y}_{c0}$ and $\bar{y}_{c1}$ becomes

$$E_{12} = \frac{1}{4}\bar{y}_c^2 = \frac{1}{4}(\bar{y}_{c0}^2 + 2N_E\bar{y}_{c0}\bar{y}_{c1}) + O(N_E^2). \tag{A11}$$

Thus, the final expression for the collision efficiency up to $O(N_E)$ becomes

$$E_{12} = \exp\left(-2\int_2^\infty \frac{M-L}{rL}dr\right)\left\{1 + 2N_E\left[\exp\left(2\int_2^\infty \frac{M}{rL}dr\right) - 1\right]^{1/2} \lim_{r\to\infty}\theta_1(r)\right\} + O(N_E^2). \quad \text{(A12)}$$

REFERENCES

Ababaei, A., and B. Rosa, 2023: Collision efficiency of cloud droplets in quiescent air considering lubrication interactions, mobility of interfaces, and noncontinuum molecular effects. *Phys. Rev. Fluids*, **8**, 014102, https://doi.org/10.1103/PhysRevFluids.8.014102.

Baker, M. B., and J. G. Dash, 1989: Charge transfer in thunderstorms and the surface melting of ice. *J. Crystal Growth*, **97**, 770–776, https://doi.org/10.1016/0022-0248(89)90581-2.

——, and ——, 1994: Mechanism of charge transfer between colliding ice particles in thunderstorms. *J. Geophys. Res.*, **99**, 10 621–10 626, https://doi.org/10.1029/93JD01633.

Batchelor, G. K., 1976: Brownian diffusion of particles with hydrodynamic interaction. *J. Fluid Mech.*, **74**, 1–29, https://doi.org/10.1017/S0022112076001663.

——, 1982: Sedimentation in a dilute polydisperse system of interacting spheres. Part 1. General theory. *J. Fluid Mech.*, **119**, 379–408, https://doi.org/10.1017/S0022112082001402.

——, and J. T. Green, 1972: The hydrodynamic interaction of two small freely-moving spheres in a linear flow field. *J. Fluid Mech.*, **56**, 375–400, https://doi.org/10.1017/S0022112072002927.

Bhalwankar, R., V. Pawar, and A. K. Kamra, 2023: Binary collisions of water drops in presence of horizontal electric fields: A wind tunnel study. *J. Geophys. Res. Atmos.*, **128**, e2022JD037543, https://doi.org/10.1029/2022JD037543.

Bhalwankar, R. V., and A. K. Kamra, 2007: A wind tunnel investigation of the deformation of water drops in the vertical and horizontal electric fields. *J. Geophys. Res.*, **112**, D10215, https://doi.org/10.1029/2006JD007863.

——, and ——, 2009: A wind tunnel investigation of the distortion of polluted water drops in the horizontal electric fields. *J. Geophys. Res.*, **114**, D10205, https://doi.org/10.1029/2008JD011102.

Chen, S., M. K. Yau, and P. Bartello, 2018: Turbulence effects of collision efficiency and broadening of droplet size distribution in cumulus clouds. *J. Atmos. Sci.*, **75**, 203–217, https://doi.org/10.1175/JAS-D-17-0123.1.

Chun, J., D. L. Koch, S. L. Rani, A. Ahluwalia, and L. R. Collins, 2005: Clustering of aerosol particles in isotropic turbulence. *J. Fluid Mech.*, **536**, 219–251, https://doi.org/10.1017/S0022112005004568.

Dash, J. G., and J. S. Wettlaufer, 2003: The surface physics of ice in thunderstorms. *Can. J. Phys.*, **81**, 201–207, https://doi.org/10.1139/p03-011.

——, B. L. Mason, and J. S. Wettlaufer, 2001: Theory of charge and mass transfer in ice-ice collisions. *J. Geophys. Res.*, **106**, 20 395–20 402, https://doi.org/10.1029/2001JD900109.

Davis, M. H., 1964: Two charged spherical conductors in a uniform electric field: Forces and field strength. *Quart. J. Mech. Appl. Math.*, **17**, 499–511, https://doi.org/10.1093/qjmam/17.4.499.

Davis, R. H., 1984: The rate of coagulation of a dilute polydisperse system of sedimenting spheres. *J. Fluid Mech.*, **145**, 179–199, https://doi.org/10.1017/S002211208400286X.

——, J. A. Schonberg, and J. M. Rallison, 1989: The lubrication force between two viscous drops. *Phys. Fluids*, **1**, 77–81, https://doi.org/10.1063/1.857525.

Devenish, B. J., and Coauthors, 2012: Droplet growth in warm turbulent clouds. *Quart. J. Roy. Meteor. Soc.*, **138**, 1401–1429, https://doi.org/10.1002/qj.1897.

Dhanasekaran, J., A. Roy, and D. L. Koch, 2021a: Collision rate of bidisperse, hydrodynamically interacting spheres settling in a turbulent flow. *J. Fluid Mech.*, **912**, A5, https://doi.org/10.1017/jfm.2020.1113.

——, ——, and ——, 2021b: Collision rate of bidisperse spheres settling in a compressional non-continuum gas flow. *J. Fluid Mech.*, **910**, A10, https://doi.org/10.1017/jfm.2020.942.

Dubey, A., G. P. Bewley, K. Gustavsson, and B. Mehlig, 2024: Critical charges for droplet collisions. *Phys. Rev. Fluids*, **9**, 074302, https://doi.org/10.1103/PhysRevFluids.9.074302.

Falkovich, G., and A. Pumir, 2007: Sling effect in collisions of water droplets in turbulent clouds. *J. Atmos. Sci.*, **64**, 4497–4505, https://doi.org/10.1175/2007JAS2371.1.

Friedlander, S. K., 2000: *Smoke, Dust and Haze: Fundamentals of Aerosol Dynamics.* Oxford University Press, 407 pp.

Gaskell, W., and A. J. Illingworth, 1980: Charge transfer accompanying individual collisions between ice particles and its role in thunderstorm electrification. *Quart. J. Roy. Meteor. Soc.*, **106**, 841–854, https://doi.org/10.1256/smsqj.45012.

Grabowski, W. W., and L.-P. Wang, 2013: Growth of cloud droplets in a turbulent environment. *Annu. Rev. Fluid Mech.*, **45**, 293–324, https://doi.org/10.1146/annurev-fluid-011212-140750.

Guazzelli, E., and J. F. Morris, 2011: *A Physical Introduction to Suspension Dynamics.* Cambridge Texts in Applied Mathematics, Vol. 45, Cambridge University Press, 256 pp.

Gunn, R., 1948: Electric field intensity inside of natural clouds. *J. Appl. Phys.*, **19**, 481–484, https://doi.org/10.1063/1.1698159.

Guo, S., and H. Xue, 2021: The enhancement of droplet collision by electric charges and atmospheric electric fields. *Atmos. Chem. Phys.*, **21**, 69–85, https://doi.org/10.5194/acp-21-69-2021.

Hamaker, H. C., 1937: The London—van der Waals attraction between spherical particles. *Physica*, **4**, 1058–1072, https://doi.org/10.1016/S0031-8914(37)80203-7.

Jayaratne, E. R., C. P. R. Saunders, and J. Hallett, 1983: Laboratory studies of the charging of soft-hail during ice crystal interactions. *Quart. J. Roy. Meteor. Soc.*, **109**, 609–630, https://doi.org/10.1256/smsqj.46110.

Jeffrey, D. J., and Y. Onishi, 1984: Calculation of the resistance and mobility functions for two unequal rigid spheres in low-Reynolds-number flow. *J. Fluid Mech.*, **139**, 261–290, https://doi.org/10.1017/S0022112084000355.

Joshi, H., and A. Roy, 2025: Electrostatic interactions between anisotropic particles. arXiv, 2501.05760v1, https://doi.org/10.48550/arXiv.2501.05760.

Jost, A., M. Szakáll, K. Diehl, S. K. Mitra, A. Hundertmark, B. S. Klug, and S. Borrmann, 2019: The effect of turbulence on the accretional growth of graupel. *J. Atmos. Sci.*, **76**, 3047–3061, https://doi.org/10.1175/JAS-D-18-0200.1.

Jucha, J., A. Naso, E. Lévêque, and A. Pumir, 2018: Settling and collision between small ice crystals in turbulent flows. *Phys. Rev. Fluids*, **3**, 014604, https://doi.org/10.1103/PhysRevFluids.3.014604.

Jungwirth, P., D. Rosenfeld, and V. Buch, 2005: A possible new molecular mechanism of thundercloud electrification. *Atmos. Res.*, **76**, 190–205, https://doi.org/10.1016/j.atmosres.2004.11.016.

Kamra, A. K., 1975: The role of electrical forces in charge separation by falling precipitation in thunderclouds. *J. Atmos. Sci.*, **32**, 143–157, https://doi.org/10.1175/1520-0469(1975)032<0143:TROEFI>2.0.CO;2.

Kang, H., R. Jayaratne, and E. Williams, 2023: A new model for charge separation by proton transfer during collision between ice particles in thunderstorms. *J. Geophys. Res. Atmos.*, **128**, e2023JD038626, https://doi.org/10.1029/2023JD038626.

Khain, A., V. Arkhipov, M. Pinsky, Y. Feldman, and Ya Ryabov, 2004: Rain enhancement and fog elimination by seeding with charged droplets. Part I: Theory and numerical simulations. *J. Appl. Meteor.*, **43**, 1513–1529, https://doi.org/10.1175/JAM2131.1.

——, T. V. Prabha, N. Benmoshe, G. Pandithurai, and M. Ovchinnikov, 2013: The mechanism of first raindrops formation in deep convective clouds. *J. Geophys. Res. Atmos.*, **118**, 9123–9140, https://doi.org/10.1002/jgrd.50641.

Kim, S., and S. J. Karrila, 2013: *Microhydrodynamics: Principles and Selected Applications.* Courier Corporation, 507 pp.

Latham, J., 1981: The electrification of thunderstorms. *Quart. J. Roy. Meteor. Soc.*, **107**, 277–298, https://doi.org/10.1256/smsqj.45201.

——, and C. D. Stow, 1965: Electrification associated with the evaporation of ice. *J. Atmos. Sci.*, **22**, 320–324, https://doi.org/10.1175/1520-0469(1965)022<0320:EAWTEO>2.0.CO;2.

Lekner, J., 2011a: Near approach of two conducting spheres: Enhancement of external electric field. *J. Electrost.*, **69**, 559–563, https://doi.org/10.1016/j.elstat.2011.07.009.

——, 2011b: Polarizability of two conducting spheres. *J. Electrost.*, **69**, 435–441, https://doi.org/10.1016/j.elstat.2011.05.006.

——, 2013: Forces and torque on a pair of uncharged conducting spheres in an external electric field. *J. Appl. Phys.*, **114**, 224902, https://doi.org/10.1063/1.4845835.

Li Sing How, M., D. L. Koch, and L. R. Collins, 2021: Non-continuum tangential lubrication gas flow between two spheres. *J. Fluid Mech.*, **920**, A2, https://doi.org/10.1017/jfm.2021.308.

Mareev, E. A., and S. O. Dementyeva, 2017: The role of turbulence in thunderstorm, snowstorm, and dust storm electrification. *J. Geophys. Res. Atmos.*, **122**, 6976–6988, https://doi.org/10.1002/2016JD026150.

Mason, B. L., and J. G. Dash, 2000: Charge and mass transfer in ice-ice collisions: Experimental observations of a mechanism in thunderstorm electrification. *J. Geophys. Res.*, **105**, 10 185–10 192, https://doi.org/10.1029/2000JD900104.

Melik, D. H., and H. S. Fogler, 1984: Gravity-induced flocculation. *J. Colloid Interface Sci.*, **101**, 72–83, https://doi.org/10.1016/0021-9797(84)90009-2.

Michel, A., A. Ababaei, and B. Rosa, 2023: The influence of gravity and mass loading on the coalescence of aerodynamically interacting droplets in homogeneous isotropic turbulence. *J. Atmos. Sci.*, **80**, 2207–2220, https://doi.org/10.1175/JAS-D-22-0267.1.

Mudiar, D., S. D. Pawar, A. Hazra, M. Konwar, V. Gopalakrishnan, M. K. Srivastava, and B. N. Goswami, 2018: Quantification of observed electrical effect on the raindrop size distribution in tropical clouds. *J. Geophys. Res. Atmos.*, **123**, 4527–4544, https://doi.org/10.1029/2017JD028205.

——, ——, V. Gopalakrishnan, and E. Williams, 2021: Electric field enlarges raindrops beneath electrified clouds: Observational evidence. *Geophys. Res. Lett.*, **48,** e2021GL093577, https://doi.org/10.1029/2021GL093577.

Naso, A., J. Jucha, E. Lévêque, and A. Pumir, 2018: Collision rate of ice crystals with water droplets in turbulent flows. *J. Fluid Mech.*, **845**, 615–641, https://doi.org/10.1017/jfm.2018.238.

Patra, P., and A. Roy, 2022: Brownian coagulation of like-charged aerosol particles. *Phys. Rev. Fluids*, **7**, 064308, https://doi.org/10.1103/PhysRevFluids.7.064308.

——, D. L. Koch, and A. Roy, 2022: Collision efficiency of non-Brownian spheres in a simple shear flow—The role of non-continuum hydrodynamic interactions. *J. Fluid Mech.*, **950**, A18, https://doi.org/10.1017/jfm.2022.817.

——, ——, and ——, 2023: Collision efficiency of like-charged spheres settling in a quiescent environment. *J. Fluid Mech.*, **968**, A22, https://doi.org/10.1017/jfm.2023.544.

——, A. Roy, and J. S. Wettlaufer, 2025: Electric field effects on the collision efficiency of uncharged water droplets in a linear flow. arXiv, 2505.16010v1, https://doi.org/10.48550/arXiv.2505.16010.

Pawar, V., R. Bhalwankar, and A. K. Kamra, 2024: Effects of eccentricity and horizontal electric field on the characteristics and outcomes of binary collisions of water drops. *Geophys. Res. Lett.*, **51**, e2024GL110547, https://doi.org/10.1029/2024GL110547.

Pinsky, M. B., A. P. Khain, and M. Shapiro, 2007: Collisions of cloud droplets in a turbulent flow. Part IV: Droplet hydrodynamic interaction. *J. Atmos. Sci.*, **64**, 2462–2482, https://doi.org/10.1175/JAS3952.1.

Plumlee, H. R., and R. G. Semonin, 1965: Cloud droplet collision efficiency in electric fields. *Tellus*, **17**, 356–364, https://doi.org/10.1111/j.2153-3490.1965.tb01428.x.

Prabha, T. V., A. Khain, R. S. Maheshkumar, G. Pandithurai, J. R. Kulkarni, M. Konwar, and B. N. Goswami, 2011: Microphysics of premonsoon and monsoon clouds as seen from in situ measurements during the Cloud Aerosol Interaction and Precipitation Enhancement Experiment (CAIPEEX). *J. Atmos. Sci.*, **68**, 1882–1901, https://doi.org/10.1175/2011JAS3707.1.

Pruppacher, H. R., and J. D. Klett, 1997: *Microphysics of Clouds and Precipitation.* Kluwer Academic Publishers, 954 pp.

Rakov, V. A., and M. A. Uman, 2003: *Lightning: Physics and Effects.* Cambridge University Press, 687 pp.

Reynolds, S. E., M. Brook, and M. F. Gourley, 1957: Thunderstorm charge separation. *J. Meteor.*, **14**, 426–436, https://doi.org/10.1175/1520-0469(1957)014<0426:TCS>2.0.CO;2.

Rother, M. A., J. K. Stark, and R. H. Davis, 2022: Gravitational collision efficiencies of small viscous drops at finite Stokes numbers and low Reynolds numbers. *Int. J. Multiphase Flow*, **146**, 103876, https://doi.org/10.1016/j.ijmultiphaseflow.2021.103876.

Saffman, P. G., and J. S. Turner, 1956: On the collision of drops in turbulent clouds. *J. Fluid Mech.*, **1**, 16–30, https://doi.org/10.1017/S0022112056000020.

Sartor, J. D., 1960: Some electrostatic cloud-droplet collision efficiencies. *J. Geophys. Res.*, **65**, 1953–1957, https://doi.org/10.1029/JZ065i007p01953.

Saunders, C. P. R., 1993: A review of thunderstorm electrification processes. *J. Appl. Meteor.*, **32**, 642–655, https://doi.org/10.1175/1520-0450(1993)032<0642:AROTEP>2.0.CO;2.

——, H. Bax-Norman, C. Emersic, E. E. Avila, and N. E. Castellano, 2006: Laboratory studies of the effect of cloud conditions on graupel/crystal charge transfer in thunderstorm electrification. *Quart. J. Roy. Meteor. Soc.*, **132**, 2653–2673, https://doi.org/10.1256/qj.05.218.

Schlamp, R. J., S. N. Grover, H. R. Pruppacher, and A. E. Hamielec, 1976: A numerical investigation of the effect of electric charges and vertical external electric fields on the collision efficiency of cloud drops. *J. Atmos. Sci.*, **33**, 1747–1755, https://doi.org/10.1175/1520-0469(1976)033<1747:ANIOTE>2.0.CO;2.

Semonin, R. G., and H. R. Plumlee, 1966: Collision efficiency of charged cloud droplets in electric fields. *J. Geophys. Res.*, **71**, 4271–4278, https://doi.org/10.1029/JZ071i018p04271.

Shaw, R. A., 2003: Particle-turbulence interactions in atmospheric clouds. *Annu. Rev. Fluid Mech.*, **35**, 183–227, https://doi.org/10.1146/annurev.fluid.35.101101.161125.

Sheikh, M. Z., K. Gustavsson, E. Lévêque, B. Mehlig, A. Pumir, and A. Naso, 2022: Colliding ice crystals in turbulent clouds. *J. Atmos. Sci.*, **79**, 2205–2218, https://doi.org/10.1175/JAS-D-21-0305.1.

——, ——, E. Leveque, B. Mehlig, A. Pumir, and A. Naso, 2024: Effect of turbulence on the collision rate between settling ice crystals and droplets. *J. Atmos. Sci.*, **81**, 887–901, https://doi.org/10.1175/JAS-D-23-0119.1.

Smoluchowski, M. V., 1918: Versuch einer mathematischen theorie der koagulationskinetik kolloider lösungen. *Z. Phys. Chem.*, **92U**, 129–168, https://doi.org/10.1515/zpch-1918-9209.

Sundaram, S., and L. R. Collins, 1997: Collision statistics in an isotropic particle-laden turbulent suspension. Part 1. Direct numerical simulations. *J. Fluid Mech.*, **335**, 75–109, https://doi.org/10.1017/S0022112096004454.

Sundararajakumar, R. R., and D. L. Koch, 1996: Non-continuum lubrication flows between particles colliding in a gas. *J. Fluid Mech.*, **313**, 283–308, https://doi.org/10.1017/S0022112096002212.

Takahashi, T., 1978: Riming electrification as a charge generation mechanism in thunderstorms. *J. Atmos. Sci.*, **35**, 1536–1548, https://doi.org/10.1175/1520-0469(1978)035<1536:REAACG>2.0.CO;2.

Thiruvenkadam, N., P. Patra, V. K. Puttanna, and A. Roy, 2023: Pair trajectories of uncharged conducting spheres in an electric field. *Phys. Fluids*, **35**, 033311, https://doi.org/10.1063/5.0142014.

Tinsley, B. A., R. P. Rohrbaugh, M. Hei, and K. V. Beard, 2000: Effects of image charges on the scavenging of aerosol particles by cloud droplets and on droplet charging and possible ice nucleation processes. *J. Atmos. Sci.*, **57**, 2118–2134, https://doi.org/10.1175/1520-0469(2000)057<2118:EOICOT>2.0.CO;2.

Trinh, T. N. G., and Coauthors, 2020: Determining electric fields in thunderclouds with the radiotelescope LOFAR. *J. Geophys. Res. Atmos.*, **125**, e2019JD031433, https://doi.org/10.1029/2019JD031433.

Turner, G. J., and C. D. Stow, 2022: The effects of surface curvature and temperature on charge transfer during ice-ice collisions. *J. Geophys. Res. Atmos.*, **127**, e2021JD035552, https://doi.org/10.1029/2021JD035552.

Wallace, J. M., and P. V. Hobbs, 2006: *Atmospheric Science: An Introductory Survey*. International Geophysics Series, Vol. 92, Elsevier, 504 pp.

Wang, H., A. Z. Zinchenko, and R. H. Davis, 1994: The collision rate of small drops in linear flow fields. *J. Fluid Mech.*, **265**, 161–188, https://doi.org/10.1017/S0022112094000790.

Wang, P. K., 2013: *Physics and Dynamics of Clouds and Precipitation.* Cambridge University Press, 452 pp.

Williams, E. R., M. E. Weber, and R. E. Orville, 1989: The relationship between lightning type and convective state of thunderclouds. *J. Geophys. Res.*, **94**, 13 213–13 220, https://doi.org/10.1029/JD094iD11p13213.

Winn, W. P., G. W. Schwede, and C. B. Moore, 1974: Measurements of electric fields in thunderclouds. *J. Geophys. Res.*, **79**, 1761–1767, https://doi.org/10.1029/JC079i012p01761.

Zhang, X., and R. H. Davis, 1991: The rate of collisions due to Brownian or gravitational motion of small drops. *J. Fluid Mech.*, **230**, 479–504, https://doi.org/10.1017/S0022112091000861.

——, O. A. Basaran, and R. M. Wham, 1995: Theoretical prediction of electric field-enhanced coalescence of spherical drops. *AIChE J.*, **41**, 1629–1639, https://doi.org/10.1002/aic.690410704.

Zinchenko, A. Z., and R. H. Davis, 1994: Gravity-induced coalescence of drops at arbitrary Péclet numbers. *J. Fluid Mech.*, **280**, 119–148, https://doi.org/10.1017/S0022112094002879.